



BRNO UNIVERSITY OF TECHNOLOGY

VYSOKÉ UČENÍ TECHNICKÉ V BRNĚ

FACULTY OF MECHANICAL ENGINEERING

FAKULTA STROJNÍHO INŽENÝRSTVÍ

INSTITUTE OF PHYSICAL ENGINEERING

ÚSTAV FYZIKÁLNÍHO INŽENÝRSTVÍ

COHERENCE-GATE ASSISTED THREE-DIMENSIONAL IMAGING BY HOLOGRAPHIC MICROSCOPE

TROJROZMĚRNÉ ZOBRAZOVÁNÍ V HOLOGRAFICKÉM MIKROSKOPU POMOCÍ KOHERENČNÍ BRÁNY

MASTER'S THESIS

DIPLOMOVÁ PRÁCE

AUTHOR

AUTOR PRÁCE

Bc. Barbora Maršíková

SUPERVISOR

VEDOUCÍ PRÁCE

prof. RNDr. Radim Chmelík, Ph.D.

BRNO 2018

Master's Thesis Assignment

Institut: Institute of Physical Engineering
Student: **Bc. Barbora Maršíková**
Degree program: Applied Sciences in Engineering
Branch: Precise Mechanics and Optics
Supervisor: **prof. RNDr. Radim Chmelík, Ph.D.**
Academic year: 2017/18

As provided for by the Act No. 111/98 Coll. on higher education institutions and the BUT Study and Examination Regulations, the director of the Institute hereby assigns the following topic of Master's Thesis:

Coherence-gate assisted three-dimensional imaging by holographic microscope

Brief description:

The use of coherence gating in coherence-controlled holographic microscope results in attenuation of some spatial frequencies of the image, when the object is defocused. This improves the axial localization of sample details and creates an optical section through a three-dimensional sample. The simulations show that the effect is stronger with the lower spatial coherence of the illumination, i.e. with the higher numerical aperture of condenser lenses.

Master's Thesis goals:

1. Determination of sample-details axial-localization dependence on the numerical aperture of condenser lenses by numerical simulation.
2. Design and realization of the microscope adaptation for the use of condenser optics with higher numerical aperture and lower optical aberrations.
3. Experimental verification of simulation results.

Recommended bibliography:

BORN, M., WOLF, E., Principles of Optics, 7th Exp.Ed. Cambridge Univ. Press, Cambridge 2002.

CHMELÍK, R., SLABÁ, M., KOLLÁROVÁ, V., SLABÝ, T., LOŠŤÁK, M., ČOLLÁKOVÁ, J., DOSTÁL, Z., The Role of Coherence in Image Formation in Holographic Microscopy, PROGRESS IN OPTICS, Vol. 59 (2014), pp. 267-335.

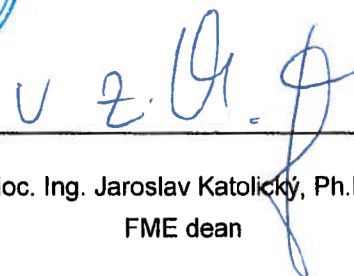
SLABÝ, T., KOLMAN, P., DOSTÁL, Z., ANTOŠ, M., LOŠŤÁK, M., CHMELÍK, R., Off-axis setup taking full advantage of incoherent illumination in coherence-controlled holographic microscope, OPTICS EXPRESS, Vol. 21, No. 12 (2013), pp. 14747-14762.

Students are required to submit the thesis within the deadlines stated in the schedule of the academic year 2017/18.

In Brno, 7. 11. 2017



prof. RNDr. Tomáš Šikola, CSc.
Director of the Institute



doc. Ing. Jaroslav Katolický, Ph.D.
FME dean

Abstrakt

Tato diplomová práce se zabývá výzkumem na téma vlivu prostorové koherence osvětlení. Účelem je určit schopnost osové lokalizace při zobrazení Koherencí řízeným holografickým mikroskopem (CCHM) v závislosti na různé prostorové koherenci světelného zdroje. Osová lokalizace je v tomto případě zkoumána jako kvalita rozlišení drobných detailů trojrozměrného vzorku, umístěných nad sebou. Teorie zobrazení holografickým mikroskopem a teorie rozptylu v nehomogenních prostředích je shrnuta v první části práce, v rozsahu nutném pro pochopení části praktické. Základní princip fungování mikroskopu a přesný popis jeho uspořádání je zde podrobně popsán. Proběhl mechanický návrh stavební úpravy mikroskopu tak, aby bylo možno využívat kondenzorovou optiku s vysokou numerickou aperturou a omezenými optickými vadami. Několik různých přístupů, které by mohly vést ke zlepšení zobrazovacích vlastností mikroskopu, bylo navrženo a vyzkoušeno a jsou zde popsány i s jejich výhodami a nevýhodami. Pro experimentální část práce byl vyroben modelový vzorek. Závislost osové lokalizace na prostorové koherenci osvětlení byla demonstrována pomocí simulace a následně ověřena experimentálně, pozorováním vyrobeného modelového vzorku. Experimentální výsledky potvrzují základní principy vycházející ze zmíněné teorie. Na závěr jsou navržena možná vylepšení, pro budoucí zpřesnění výsledků.

Abstract

This master thesis covers the primary research on the influence of spatially incoherent illumination on the axial localization of small details in a three-dimensional sample. The imaging is done by the coherence-controlled holographic microscope (CCHM). The necessary theory of imaging and scattering is summarized in the theoretical part. The fundamental principle as well as the actual setup of the microscope is described in detail and a mechanical adaptation is designed for the use of condenser optics with high numerical aperture and low aberration. For the experimental part, a model sample has been prepared and measured. The relationship between the spatial incoherence of illumination and the axial localization is demonstrated on simulations and verified experimentally using the model sample. The experiments prove the basic idea of the theory. In the end, some improvements are suggested for the future research on this topic.

Klíčová slova

Holografická mikroskopie, kvantitativní fázové zobrazení, trojrozměrné zobrazení, optické řezy, koherenční brána, prostorově nekoherentní osvětlení.

Keywords

Holographic microscopy, quantitative phase imaging, three-dimensional imaging, optical sectioning, coherence gating, spatially incoherent illumination.

MARŠÍKOVÁ, B. *Trojrozměrné zobrazování v holografickém mikroskopu pomocí koherenční brány*. Brno: Vysoké učení technické v Brně, Fakulta strojního inženýrství, 2018. 62 s. Vedoucí diplomové práce prof. RNDr. Radim Chmelík, Ph.D.

Declaration

I declare that the master thesis submitted hereby is my own work under supervision of prof. RNDr. Radim Chmelík, Ph.D., and that all literature sources were quoted completely and correctly.

.....

Brno, 25th May 2018

First of all, I'd like to thank prof. RNDr. Radim Chmelík, Ph.D. for supervising my thesis, for his mentoring and valuable advice. Besides, I'd like to thank prof. RNDr. Jiří Petráček, Dr. for providing the simulations of three-dimensional imaging, Ing. Zbyněk Dostál, Ph.D. for the help with the technical part of my thesis and Ing. Hana Uhlířová, Ph.D. and Ing. Lenka Štrbková, Ph.D. for the collaboration on the sample preparation.

Table of contents

Introduction	3
1 Quantitative phase imaging in holographic microscopy	5
2 Coherence-controlled holographic microscope	7
2.1 Illumination part	8
2.2 Imaging part	9
2.3 Recording and reconstructing a hologram	11
3 Optical sectioning with CCHM	13
3.1 Incoherence of the illumination	13
3.2 Defining the coherence of light	14
3.3 Coherence gating	14
3.4 Influence on imaging properties	15
4 Theory of imaging by CCHM	17
4.1 Two-dimensional imaging	17
4.2 Three-dimensional imaging	19
4.2.1 Angular spectrum of a light wave	19
4.2.2 Imaging by an optical system	20
4.2.3 Illumination source	21
4.2.4 Point spread function	22
4.2.5 The three-dimensional coherent transfer function	22
5 Simulations	25
5.1 Scattering from inhomogeneous media	25
5.1.1 The first-order Born approximation	27
5.1.2 The Rytov approximation	28
5.2 Theoretical simulation	30
5.3 Sample preparation	33
5.4 Simulation of the prepared hydrogel sample	35
6 Experiments and results	37
6.1 Sample quantification	37
6.2 Axial localization with original condenser optics	38
6.3 Microscope adaptation for the use of condenser optics with high numerical aperture	39
6.3.1 Positioning of the condensers	40
6.3.2 The mechanical design and adaptation for objectives	42
6.3.3 The 40× objectives in the condenser position	44
6.3.4 The final version of microscope adaptation	45
6.3.5 The process of microscope adjustment	47

6.4	Improvement in lateral resolution	48
6.5	Improvement in axial localization	49
	Conclusion	57
	References	59

Introduction

The coherence-controlled holographic microscope (CCHM) became a powerful tool in biological imaging [1, 2], for example for tumour cells observations which is done in our lab, but also for many other applications, either medical or technical. However, there is always space for improvement. This thesis is discussing the issues of three-dimensional imaging which is an important topic and further progress would be beneficial for the quantitative phase imaging used in medicine and biology.

Nowadays, most biological samples are observed in two dimensions only, placed between a microscope slide and a cover slip. But this is no natural environment for cells. If we stick to the example of tumour cells, those are usually crawling through the tissues they attack. To observe such phenomena in a microscope, it would be necessary to achieve a very good axial localization, to be able to precisely track the cell not only in xy plane but also in z direction. As the theory of image formation in a holographic microscope suggests, low coherence of the illumination creates the coherence gate effect, which then results in optical sectioning, because the defocused light does not contribute to the interference pattern on the detector. It has been observed previously, that lowering the spatial coherence of the illumination improves the lateral resolution and also the axial localization of the details in a small phase object (i. e. a cell) [3]. It is the motivation of this master thesis to prove the latter statement and show, that three-dimensional quantitative phase imaging can benefit from high numerical aperture of the illumination.

There are three important goals that should be reached in this thesis:

- determination of sample-details axial-localization dependence on the numerical aperture of condenser lenses by numerical simulation,
- design and realization of the microscope adaptation for the use of condenser optics with higher numerical aperture and lower optical aberrations,
- experimental verification of simulation results.

During the work on this thesis, the above tasks were confronted. The process of solving these questions and the solutions, together with literature research, became the content of this thesis.

The first chapter is a short introduction to quantitative phase imaging (QPI) and its importance in observing live cells. Second, more technical part, is dedicated to the coherence-controlled holographic microscope, especially the illumination part that needed to be adapted. It is followed by two theoretical chapters about imaging theory of CCHM and optical sectioning. This gives introduction to the Chap. 5 where the first goal of this thesis is reached. It includes both the theory and the simulations that were used as a reference for the experiment. The last part shows the experimental results and the contribution of the author. The adaptation requirements for high NA condenser optics, which was one of the tasks, is also described there.

1 Quantitative phase imaging in holographic microscopy

The light microscopy is one of the significant inventions of human history. Many advanced techniques have been developed through the past centuries. Most of the progress is devoted to improvement of the two main properties: resolution and contrast. The theoretical resolution limit has been defined by Abbe as approximately half the wavelength [4]. Since then, light microscopy was trying to reach this limit by aberration correction etc. In the past decades, so-called superresolution techniques were developed, capable of exceeding this limit [5].

For contrast imaging, it is important to distinguish between amplitude and phase contrast. All the common detectors, either camera chips, photographic material or human eyes, are sensitive to the intensity of the light, which equals to the square of amplitude modulus of the light wave. On the contrary, phase objects do not really affect the amplitude of light, i. e. the intensity that can be measured, but often only its phase. Therefore, they have very low contrast in bright field microscopy imaging. In cell biology, the specimens are almost exclusively phase objects. Many microscopy methods have been developed to convert the phase change into the amplitude change, which can be easily detected. Such methods, for example Zernike's phase contrast [6] or Nomarski's differential interference contrast (DIC) [7], enable for phase observation but neither of them is quantitative and hence no direct phase measurement is possible.

The property called *quantitative phase imaging* (QPI) became feasible with the invention of interference microscopy methods. In the 1940s, Dennis Gabor proposed holography as an approach for exploiting the phase information [8]. He suggested an option for possible resolution improvement for electron microscopy. His method consisted of two steps. Firstly, the interference of a coherent electron beam with its part diffracted on the sample is recorded. This record is called a hologram and in the second step is used to reconstruct the phase information when being illuminated by a light wave. The experiments were unsuccessful, due to low coherence of electron sources and high aberrations back then [9].

After the invention of laser, a light source capable of extremely high degree of coherence, there was a huge progress in holography and an off-axis holographic system [10] has been proposed as an alternative to the original Gabor's in-line arrangement. Later very fast development of digital image acquisition and image processing helped to ease the treatment of holographic data and digital holography found its place as one of the quantitative phase imaging methods for non-invasive observation and measuring of biological samples.

Coherence-controlled holographic microscopes developed at the Institute of Physical Engineering of Faculty of Mechanical Engineering, B U T, are off-axis interference microscopes with unique design, allowing for the use of spatially and temporally incoherent light. With CCHM, quantitative phase imaging is possible even for very fast processes, which are of interest in biology of cells and tissues. The lateral resolution is comparable

to conventional microscopes and special properties, such as coherence gating and optical sectioning are available. Also the label-free imaging, non-invasiveness of holographic microscopy and possibility of live-cell imaging are great advantages of this approach. The phase distribution captured by CCHM can be easily converted to cell dry mass per area [1].

CCHM has been previously used to study human cancer cells [1] in two dimensions on a microscope slide and also to observe the cell movement in three-dimensional extracellular matrix [11]. Cancer cells possess a wide range of migration and invasion mechanisms. Better understanding of how cancer cells disseminate could lead to new treatment methods. For that, it would be beneficial to study the cellular basis of the different types of migration and invasion. Cell activity and its interaction with the collagen matrix, or other material of interest, can be imaged by CCHM. Thanks to the low degree of coherence of illumination that the microscope is able to maintain, the presence of the optically thick material does not considerably influence the imaging quality. Time-lapse records can be obtained for the study of cell dynamics and interactions [11].

Three-dimensional quantitative phase imaging is of particular interest in cell biology, since the two-dimensional model situation does not fully resemble the situation *in vivo*. The improvement of three-dimensional imaging in weakly scattering matrices would enable better modelling of the cell's natural habitat *in vitro*. Knowing the effects of changing the degree of coherence is significant for reasons described in the following chapters.

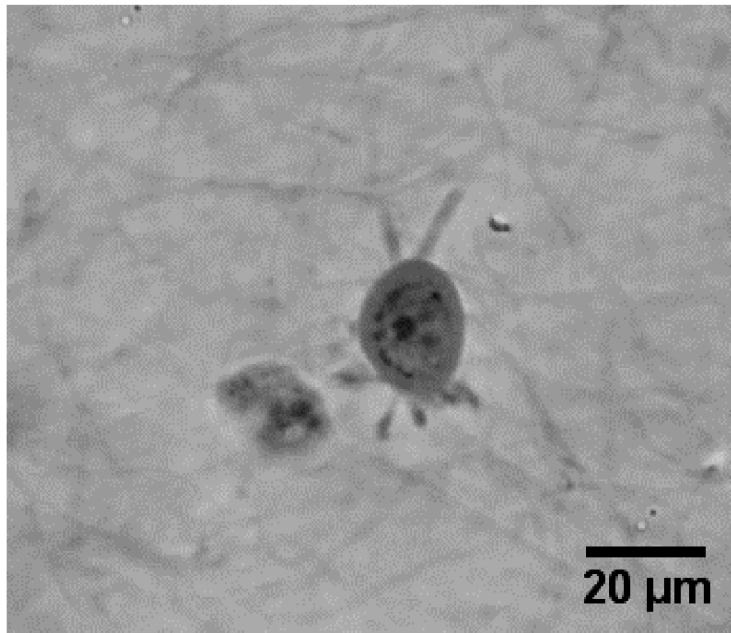


Figure 1: Quantitative phase image of human sarcoma cell in collagen gel; both the cell and collagen fibres are visible, but the fibres do not disturb the image considerably [11].

2 Coherence-controlled holographic microscope

The name ‘‘Coherence-controlled holographic microscope’’ was first introduced in 2010 [12] and reflects the crucial ability of the microscope to control its imaging properties by changing the degree of spatial and temporal coherence of the illuminating light. It combines an off-axis holographic configuration and an achromatic grating interferometer that allows for the use of arbitrary degree of coherence. This system is combining principles of in-line and off-axis holography in such a way that it benefits from the advantages while simultaneously eliminating the disadvantages of both of them. CCHM is therefore able to produce real-time optically sectioned quantitative phase contrast images, which does not suffer from the issues of coherent imaging, such as speckles, unwanted interference and diffraction [13].

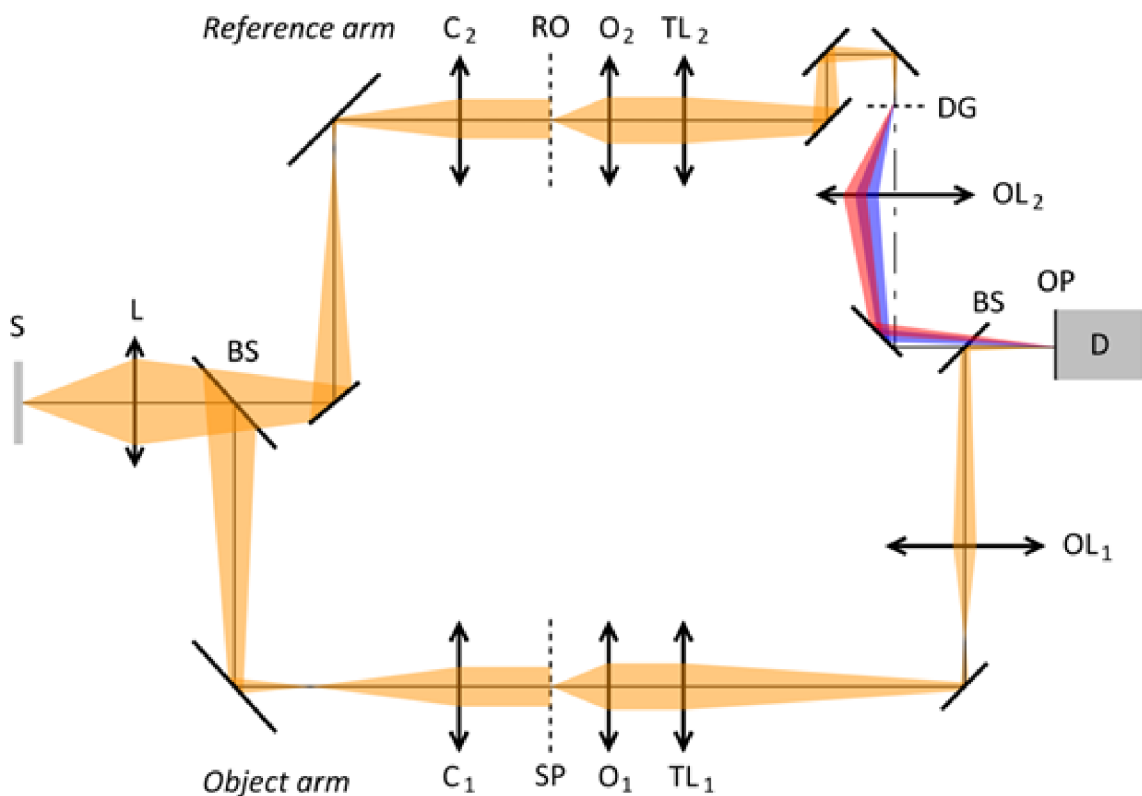


Figure 2: Optical setup of the microscope: Light source (S), relay lens (L), beam splitters (BS), condensers (C), specimen plane (SP), reference plane (RO), objectives (O), tube lenses (TL), diffraction grating (DG), output lenses (OL), output plane (OP), detector (D) [11].

The latest design of CCHM is a Mach-Zehnder-type interferometer adapted for achromatic off-axis holography. Achromatic-fringe interference systems were introduced already in 1960s [10], and the possibility of using partially coherent light was described. Lowering the coherence of illumination brings the advantages of reduction of coherence noise, possibility of observation through scattering media and improvement in depth discrimination

thanks to the effect of coherence gating [14]. Illuminating with low degree of coherence also increases the lateral resolution [3, 15]. To achieve achromaticity, diffraction grating is placed in the reference arm, like in other similar setups [16].

The basic setup is displayed in fig. 2. Here, the version of the setup for transmitted-light with transmission diffraction grating is described, because it was used in the experimental part. The use of transmission diffraction grating is convenient, because it limits the light losses, compared to the original setup with reflection grating [11, 13].

2.1 Illumination part

Light from the light source (S), which first passes through a replaceable bandpass filter, is split by the beam splitter (BS) into the reference arm and object arm. Both arms are composed of identical components, namely the condensers (C), objectives (O) and tube lenses (TL). The light source is a halogen lamp coupled into a light guide, $\varnothing 5$ mm, with an interference filter $\lambda = 650$ nm, 10 nm FWHM attached. After the splitting, both beams pass through a series of mirrors to reach the back focal planes of the condensers. The Köhler illumination, working on the classical principle [17], is achieved by the relay lens. More precisely, as shown in fig. 3, it is a series of two lenses working together as a collimator. Thanks to that, both the specimen (SP) and the reference plane (RO) are illuminated uniformly.

From fig. 3 it is obvious that the collimator lenses focus the light into the condenser aperture in such way that it is filled completely, when the aperture diaphragm is fully open, the diameter of illuminated area being 28 mm. The condenser of CCHM is Nikon Ti-C-LWD, LWD and as mentioned before, two identical condensers are used, each in one arm (C_1, C_2). The condensers have numerical aperture $NA = 0.52$ but currently in the setup we work with, due to optical aberrations and misalignment of the system, the highest NA_S , illumination numerical aperture, that can be achieved is approximately 0,3. The value of NA_S is the lowest one of the following three: the numerical aperture of the condenser, the aperture diaphragm, which is limiting the light coming to the condenser's back focal plane, and the numerical aperture of the objective [15].

With the proper microscope alignment, the condensers illuminate the specimen (SP) and reference plane (RO) with a plane wave for each point of the extended source. This is the goal of the microscope alignment procedure. In the standard user mode this procedure is almost completely automated [18] and included in the microscope operating software, but for the special purpose can also be executed step by step. The important part of the alignment is finding the right working distance of the condenser. This is done by focusing the image of almost closed field aperture (FA) in fig. 3 onto the specimen plane (SP). The precise working distance needed may be slightly different for the object and reference arm, so a relative focus positioning is introduced for focusing the image of the field aperture in the reference plane (RO) as well.

The use of illuminating condensers is one of the two properties that distinguish this setup from the first generation CCHM [12]. There, four identical objective lenses were

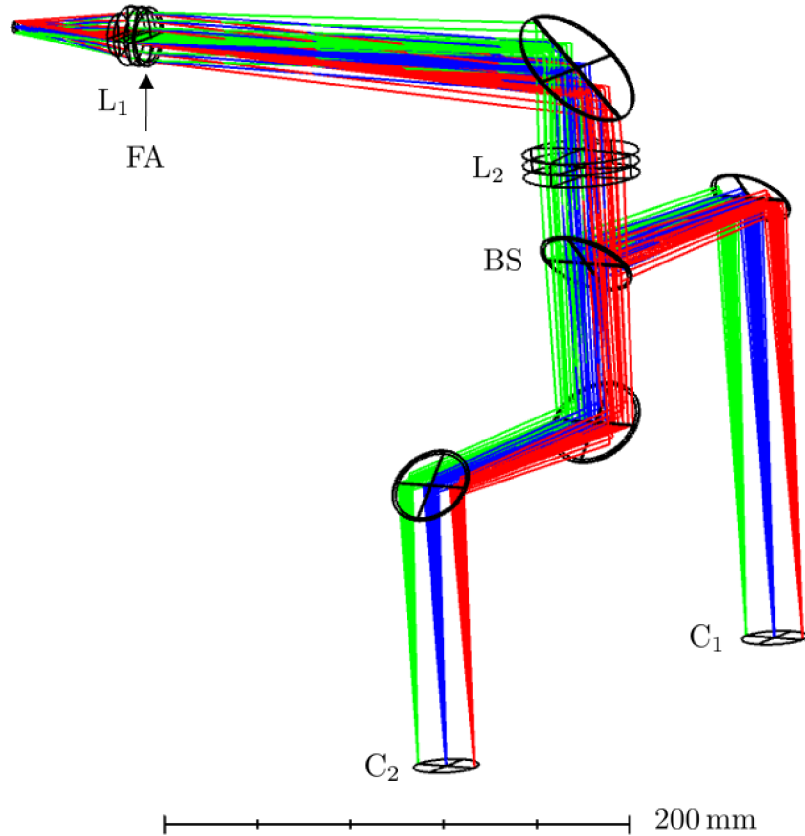


Figure 3: Zemax simulation of the real illumination setup of CCHM. Blue depicts the optical path of central ray, red and green are the rays from the margin of the light source, each 2.5 mm from the central ray.

used, two of them for illumination, serving as condensers, and the other two for imaging. This setup had a limitation given by the low working distance of the objectives and thus the lack of working space between the condenser and the objective, even though long working distance lenses were employed. This was improved in the second generation setup, described here, but at the cost of losing the possibility to use very low degree of spatial coherence of the illumination, since the condensers have more optical aberrations than the microscope objectives of the same NA. Also, the economical aspect played its role, considering the costs of four identical objectives for each magnification [13].

2.2 Imaging part

Both the specimen and the reference object are observed by a microscope system realized as a combination of infinity corrected objectives (O_1 , O_2) and tube lenses (TL_1 , TL_2). Various objectives with different magnification can be used and the change of magnification is simple, thanks to two simultaneously rotating carousels carrying the objectives. The crucial component of CCHM is the diffraction grating (DG), placed in the reference arm

and imaged into the output plane (OP) as proposed earlier [19]. The object and reference planes (SP, RO) and the diffraction grating plane (DG) are optically conjugated together with the output plane (OP) by the objectives (O_1, O_2) and the output lenses (OL_1, OL_2). Only the $+1^{\text{st}}$ order of the diffraction grating is transmitted to the output plane and used for imaging, to preserve the best possible contrast of the interference pattern, the rest is eliminated by spatial filtering in focal plane of the reference output lens (OL_2). Therefore, the image of the grating is not formed by the reference beam in the output plane. But when the object beam recombines with it in the output plane, the interference fringe pattern appears. The frequency of this hologram correspond to the frequency of the diffraction grating grooves as if it was formed by the 0^{th} and $+1^{\text{st}}$ order of this grating. The spatial frequency of the interference fringes, the *carrier frequency*, equals to the spatial frequency of the diffraction grating grooves reduced by the magnification of the output lens (OL_2):

$$f_c = \frac{f_G}{m_{OL}}, \quad (1)$$

where f_c is the carrier frequency, f_G is the diffraction grating frequency and m_{OL} is the magnification of the output lens (OL_2).

The use of the diffraction grating is fundamental for the interferometer unit. The axial ray incident onto the diffraction grating is diffracted by this grating to its 1^{st} diffraction order at the angle α given by the grating equation $\sin(\alpha) = \lambda f_G$, where λ is the wavelength of the incident ray. Since the diffraction grating plane is imaged by the output lens (OL_2) into the output plane of the microscope system, each ray diffracted at the angle α , which passes through the lens, enters the output plane at angle β that fulfils the condition $\sin(\beta) = \sin(\alpha)/m_{OL}$. Because of the dispersion caused by the diffraction grating, rays of each wavelength are entering the output plane at such an angle β that, for all the wavelengths, an interference pattern of the same spatial frequency is generated in the output plane. Therefore, when partially coherent or incoherent light source is used, the achromatic-fringe hologram of the specimen is formed in the output plane. The orientation of the interference fringes is parallel to the one of the diffraction grating grooves [13, 20].

The way of employment of the diffraction grating is the main important difference between the first and second generation of CCHM. In the previous design, the diffraction grating has been used as a beam splitter to split the incident light into the object beam and reference beam. This optical setup however had limited spectral transmittance for wavelengths different from the central one. This was the consequence of the dispersive power of the diffraction grating and it negatively affected the signal quality at these wavelengths.

The objectives used for all the experiments in Chap 6 were Nikon CFI Plan Fluor $20 \times / 0.5$ with working distance $WD = 2.1$ mm. Usually, for easier localization of the samples also Nikon CFI Plan Fluor $10 \times / 0.3$ with working distance $WD = 16.0$ mm were used.

2.3 Recording and reconstructing a hologram

The hologram is recorded on the detector (D) and the image is reconstructed in real time by a computer. The detector is a black and white CCD chip with pixel pitch $6.45 \mu\text{m}$. Because of the use of CCD for detection, it is highly desirable to employ plan-corrected optics for the imaging part, not just for the objectives but also for the tube lenses and output lenses.

The detector is only capable of recording the intensity (I) but the hologram carries the information about the phase as well. Let's note the image complex amplitude distribution of the object $O(x, y)$ and the reference $R(x, y)$. Then the intensity distribution of the hologram, which is generated in the output plane by the interference of those two waves, is equal to

$$\begin{aligned} I(x, y) &= |O(x, y) + R(x, y)|^2 = \\ &= |O|^2 + |R|^2 + OR^* + O^*R, \end{aligned} \quad (2)$$

where the asterisk denotes the complex conjugate operator and x, y are the coordinates in the output plane. The first term in the second row corresponds to the intensity of the object wave, the second one to the reference wave intensity. Those two create so-called 0th order in the spatial frequency spectrum of the hologram, the central area of fig. 4 (b). The image term is OR^* and O^*R is its complex conjugate and they create the +1st and -1st order. Both of them can be used for reconstruction of the object amplitude and phase.

The process of reconstruction is based on carrier frequency removal in the Fourier plane [21,22]. The hologram is Fourier transformed by the 2D fast Fourier transform (FFT) algorithm. The image spectrum is then extracted by a windowing operator. The window is centred at the carrier frequency f_c and its size corresponds to the maximum image term spatial frequency f_{MAX} . This spatial frequency is in CCHM given by

$$f_{\text{MAX}} = \frac{\text{NA} + \text{NA}_S}{m\lambda} \leq \frac{2\text{NA}}{m\lambda}, \quad (3)$$

where NA is the numerical aperture of the objectives, NA_S is the illumination numerical aperture, m is the total magnification between the output plane and the specimen plane of the objectives and λ is the wavelength of illuminating light. The origin of the frequency is translated to the centre of the window and the spectrum is multiplied by an apodization function. By the use of 2D inverse fast Fourier transform the holographic signal of the image is computed. It is the product of object complex amplitude and reference complex amplitude. Finally, the image amplitude is derived as the modulus of the holographic signal and the phase is derived as its argument.

The phase image represents the optical path difference (OPD) caused by the specimen and its values are wrapped on the interval $\langle -\pi, \pi \rangle$. Thus an unwrapping procedure needs to be applied to obtain a smooth phase image without phase steps. There is also a distortion in the phase image, caused by aberration of the optical elements of the microscope, so a flat-field compensation of the image is necessary. These procedures are

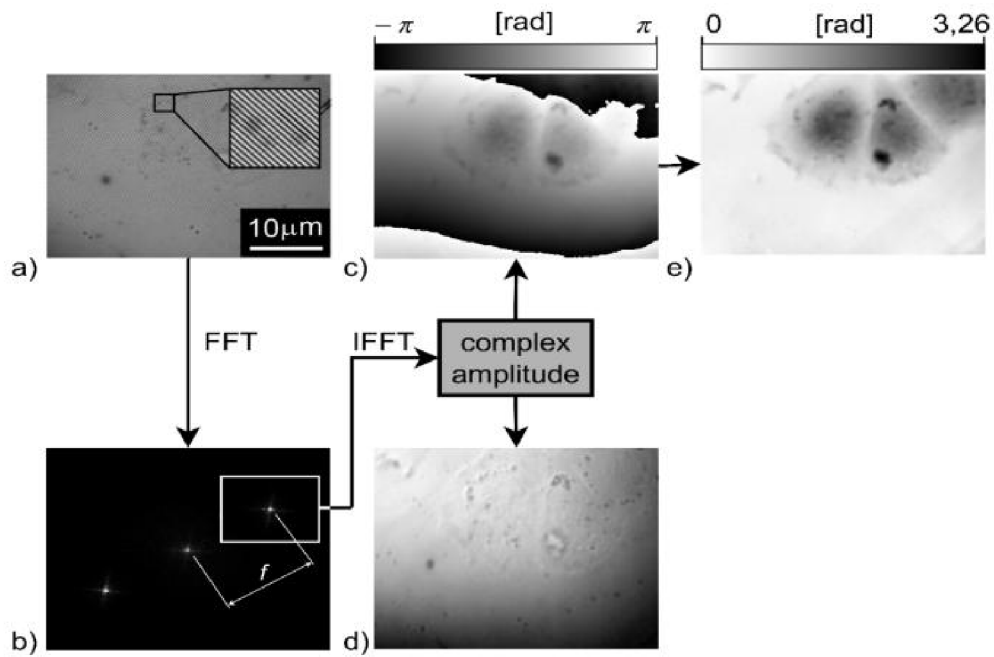


Figure 4: Image processing: (a) a hologram, (b) spatial frequency spectrum, the image spectrum (the $+1^{\text{st}}$ order) in the frame, (c) the phase image, (d) the amplitude image and (e) compensated phase [18].

included in the operating software, so the user can not only see the real time hologram, but the amplitude, raw phase and compensated phase image as well. All of these may be saved by capturing the image and choosing to save them separately, but it is enough to store the holograms, since everything else is derived from them [20].

3 Optical sectioning with CCHM

The term “optical sectioning” refers to the selective imaging of a single planar section of a three-dimensional object, where the out-of-focus light is rejected. In conventional imaging with high numerical aperture objectives only a single plane is focused on the detector. However, the information from the other planes also arrives to the detector and creates blurry images overlapping the focused image [23]. Imaging of a plane embedded within a thick specimen is an important problem of modern microscopy imaging techniques. In biological microscopy, even the thin cells and tissues are often considered thick, compared to the depth of focus [24].

Many interferometric systems have been designed for phase measurement, but only some provide the possibility of optical sectioning [23, 24]. If we take a look at the basic classification of interferometric systems, we have two groups to compare. Firstly, there are in-line systems, characterized by the zero angle between the object and the reference beam. Optical sectioning is possible with them, by the coherence gating effect due to the use of low-coherence light source. These systems, however, require more than one interferogram for the reconstruction of the object wave. On the other hand, off-axis systems are characterized by a non-zero angle between the object and reference beam. These systems are often called digital holographic microscopes (DHM). One captured image, which is then called hologram, is enough for the object wave reconstruction in their case but the use of incoherent light source is not allowed. Thus optical sectioning is not available and also the coherence noise manifests in the images.

The coherence-controlled holographic microscope combines the principles of both systems and therefore possess the important ability of optical sectioning. The confocal-like optical sectioning property of CCHM system was already proved both theoretically and experimentally for the reflected-light arrangement [21]. This property seems to be beneficial for imaging in diffusing media [25]. Shortly, CCHM enables off-axis holographic microscopy with completely temporally and spatially incoherent light source and therefore is providing real time speckle-free optically sectioned quantitative phase contrast imaging.

3.1 Incoherence of the illumination

Low coherence of illumination very effectively eliminates coherence noise and various coherence artefacts and improves lateral resolution of holographic microscope [26]. The experimental verification of the lateral resolution improvement is well-documented [3, 13]. Another very important effect of low coherence is the coherence gating effect that enables optical sectioning and therefore allows imaging of objects under diffusing layers or immersed in turbid media [27–29].

We can assume that a thick object, such as a collagen gel [11] or hydrogel (see Chap. 5.3), behaves similarly. In fact, we can consider the out-of focus layers of this thick object to influence the imaging the same way like a diffusing layer influences the imaging of a thin (two-dimensional) sample.

3.2 Defining the coherence of light

Two waves, which have a constant phase difference and the same frequency and waveform, are coherent. Generally, high coherence of two or more wave enables their interference. Spatial coherence describes the coherence of two waves coming from different points of the light source. We can observe it in Young's double slit experiment, where the interference disappears if the slits are too far from each other. Temporal coherence is the correlation between a wave and its time-delayed version. This is best explained on the example of Michelson interferometer. By moving the mirror in one arm, the contrast of the interference fringes fades away once the optical path difference is too long [30].

In CCHM, temporal coherence is affected by the bandpass filter that is placed directly after the source (the light guide). Spatial coherence is changed by varying the numerical aperture NA_S of the condensers, i. e. closing its aperture diaphragm.

The coherence of a light wave may be described by the values of coherence width (CW) and coherence length (CL). Estimated CW is the diameter of a circular area that is illuminated almost coherently. The CL can be calculated as $d_l = \lambda^2/\Delta\lambda$ [31], where $\Delta\lambda$ is FWHM of the spectral function of the light source, i. e. of the bandpass filter attached. The lower is the spatial or temporal coherence, the lower is CW and CL respectively [13]. The coherence volume is a product of coherence length and coherence area, which is coherence width squared [32].

From another point of view, we can characterize the optical system of the microscope by the numerical aperture NA of the objective lenses and by the numerical aperture NA_S of the condensers. Then, we can describe the spatial coherence of the illumination by the *partial coherence factor* $\sigma = NA_S/NA$. For $\sigma = 1$ the spatial coherence of the illumination is minimal, for $\sigma \rightarrow 0$ we consider the illumination coherent [3].

3.3 Coherence gating

Thanks to the possibility to use the temporally and spatially incoherent illumination, CCHM allows for the use of coherence gating effect. This means that the contribution of the light scattered at all the out-of-focus planes is limited and does not affect the resulting images significantly. When both spatial and temporal coherence is limited in CCHM, it results in improvement of the in-focus image contrast, which is most beneficial for imaging thick objects or objects in scattering media [13].

In the situation of reflected light mode of CCHM we can say that the coherence gating creates a real confocal effect. Generally, the light travels through the object and reference arm. If it's scattered in the specimen plane in the object arm, it will fall into the coherence volume in the output plane and interfere. The light scattered outside the specimen plane will not arrive to the coherence volume, therefore, no interference is possible. This effect is enhanced for the reflected light arrangement, because the light scattered in a different plane has significantly different path length. In the situation of transmitted light configuration, the path length of a photon does not change significantly when scattered

in different plane. For this reason, reduction of both spatial and temporal coherence has significant gating effect in reflected-light arrangement.

In transmitted light arrangement, mostly the reduction of spatial coherence leads to the effect of coherence gating. This can be explained by the relationship between the form of the mutual-coherence function of the object and reference arm and the characteristics of the source [24]. A spatially broad, spectrally narrow light source forms the coherence function that is narrow in the transverse spatial dimension and prolonged in the temporal dimension. On the other hand, a spatially narrow and spectrally broad source forms the coherence function with opposite parameters. Light that is scattered from outside the focused plane results in the transverse shift of the point of incidence in the image plane, but it is not substantially delayed in time. This is the main reason why the coherence gating is a consequence of spatial broadening of the source rather than its increased spectral width [15].

3.4 Influence on imaging properties

Since it is important for the experimental part, let's now summarize the crucial effects of coherence variations in CCHM. The degree of temporal coherence can be controlled by the use of different bandpass filters together with the white light source, the halogen lamp. The temporal coherence remains the same, for all the experiments in Chap. 6 and only the effect of spatial coherence is studied.

The degree of spatial coherence is controlled by the aperture diaphragm that changes the effective area of the extended light source. This is changed in the software by choosing the NA_S , controlling the aperture diaphragm, on a scale from 0 to 0.52, which is the theoretical maximum for the condensers used originally.

Higher coherence of illumination allows for wider axial range of numerical refocusing in holographic microscopy [15]. But it is associated with the appearance of coherence noise, speckles, diffraction on dust particles and unwanted interference. The advantage of low coherence is that all these unwanted phenomena are limited to minimum and therefore the quality is comparable to classical bright-field microscopy with incoherent illumination. In addition, the lateral resolution limit for low spatial coherence imaging is halved, compared to coherently illuminated holographic systems [15]. It also allows the coherence gating effect and therefore optical sectioning. The main disadvantage is that the numerical refocusing is possible only in a very limited axial range [33].

4 Theory of imaging by CCHM

The theory of image formation and image processing for coherence-controlled holographic microscopy has been described in detail [15]. The impact of coherence variations on the imaging properties has been explained. All of the microscope properties, important for three-dimensional imaging, that were described qualitatively in the previous chapter can be derived from this complex theoretical background. The coherence gating effect allows, in certain conditions, for real three-dimensional imaging and therefore the theory for 3D imaging is derived. The microscope imaging is characterized by means of 3D coherent transfer function (CTF), which describes the relationship between spatial frequency passband and the coherence properties of illumination.

This theory is used for microscope imaging simulation in Chap. 5 and it gives better understanding to the fundamental principles of CCHM imaging.

4.1 Two-dimensional imaging

Let's first give a simplified introduction to the imaging theory in two-dimensional approximation [3]. For imaging of a two-dimensional object, the complex holographic signal can be described as

$$w(\mathbf{q}, z) = \iint_{-\infty}^{\infty} T(\mathbf{Q}) H(\mathbf{Q}; z) \exp(i2\pi \mathbf{Q} \cdot \mathbf{q}) d^2 \mathbf{Q}, \quad (4)$$

where $\mathbf{q} = (x, y)$ is a position vector of the optically conjugated point in the object plane and $\mathbf{Q} = (X, Y)$ is a corresponding vector of spatial frequencies. The unit of \mathbf{q} is λ_v/NA , \mathbf{Q} is then in NA/λ_v units. Here, spatially low coherent quasi-monochromatic light source with wavelength λ_v in vacuum is supposed. Parameter z is an object defocus in $n\lambda_v/2\text{NA}^2$ units, which stands for half of the objective lens diffraction depth of field. The function $T(\mathbf{Q})$ is the Fourier transform of the object transmission function and $H(\mathbf{Q}; z)$ is a two-dimensional coherent transfer function, which can be approximately expressed in the form

$$H(\mathbf{Q}; z) = \iint_{-\infty}^{\infty} \text{circ}\left(\frac{Q'}{\sigma}\right) \text{circ}(|\mathbf{Q} + \mathbf{Q}'|) \exp[i\Phi z] d^2 \mathbf{Q}', \quad (5)$$

where the defined phase modulation Φ of the reference beam is

$$\Phi(z) = -2\pi \left\{ z \frac{\alpha}{q} \left[\sqrt{\alpha^2 - Q'^2} - \sqrt{\alpha^2 - (\mathbf{Q} + \mathbf{Q}')^2} \right] \right\}, \quad (6)$$

with $\alpha = n/\text{NA}$. The partial coherence factor σ , mentioned already in Chap. 3.2, is $\sigma = \text{NA}_S/\text{NA} \leq 1$. The integration domain of integral in eq. (5) is shown in fig. 5. The cut-off frequency of the system is obviously $Q_{\text{MAX}} = 1 + \sigma$.

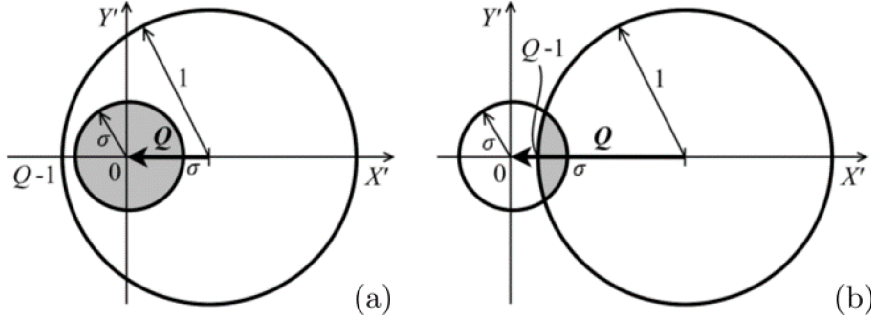


Figure 5: Integration domain is the intersection of two circles, their radii being 1 and σ , mutually shifted by the vector \mathbf{Q} ; (a) $0 \leq \mathbf{Q} \leq 1 - \sigma$, (b) $1 - \sigma \leq \mathbf{Q} \leq 1 + \sigma$ [15].

For low-NA approximation ($\text{NA} \ll 1$), we receive $\alpha \gg 1$ and the approximation of $\Phi(z)$ from eq. (6) becomes independent of α :

$$\Phi(z) \approx -2\pi \left(\mathbf{Q}^2 \frac{z}{4} + \mathbf{Q}' \cdot \mathbf{Q} \frac{z}{2} \right), \quad (7)$$

where the first term in the square brackets is independent of the integration variables X' , Y' . We then carry out the integration in eq. (5) for both cases displayed in fig. 5. The integration is straightforward for $0 \leq Q \leq 1 - \sigma$, for $1 - \sigma \leq Q \leq 1 + \sigma$ the integration domain is approximated by an inscribed circle. For $H(\mathbf{Q}; z)$ we obtain

$$H(\mathbf{Q}; z) = \begin{cases} \pi \sigma^2 \exp\left(-i\pi z \frac{Q^2}{2}\right) \frac{2J_1(v)}{v}, v = \pi \sigma Q z & \text{for } 0 \leq Q \leq 1 - \sigma, \\ \pi \left(\frac{1+\sigma-Q}{2}\right)^2 \exp\left(-i\pi z \frac{Q(1-\sigma)}{2}\right) \frac{2J_1(v)}{v}, v = \pi \frac{1+\sigma-Q}{2} Q z & \text{for } 1 - \sigma \leq Q \leq 1 + \sigma, \\ 0 & \text{otherwise.} \end{cases} \quad (8)$$

This approximation of CTF is represented by simple analytical formulas and hence it is suitable for a complex image signal $w(\mathbf{q}, z)$ deconvolution. According to eq. (8), the transfer of spatial frequency Q is suppressed for $v = v_S = 1.22\pi$, with v_S being the first root of the Bessel function $\frac{2J_1(v)}{v}$. An optical section $(-z_S, z_S)$ in the wide sense is created for the frequency \mathbf{Q} and is bounded axially by

$$z_S(Q) = \begin{cases} \frac{1.22}{\sigma Q} & \text{for } 0 \leq Q \leq 1 - \sigma, \\ \frac{2.44}{(1+\sigma-Q)Q} & \text{for } 1 - \sigma \leq Q \leq 1 + \sigma. \end{cases} \quad (9)$$

It is evident, that $z_S(Q)$ has its minimum in the first case for $Q^* = 1 - \sigma$ and in the second case for $Q^* = (1 + \sigma)/2$. When we combine these two cases, we obtain the following expression for Q^* and for $z_S^* = z_S(Q^*)$:

$$Q^* = \begin{cases} 1 - \sigma \\ \frac{1+\sigma}{2} \end{cases} \quad z_S^* = \begin{cases} \frac{1.22}{\sigma(1-\sigma)} & \text{for } 0 < \sigma < \frac{1}{3}, \\ \frac{9.76}{(1+\sigma)^2} & \text{for } \frac{1}{3} < \sigma < 1. \end{cases} \quad (10)$$

We then see that the thinnest “optical section” is formed for the frequency Q^* with thickness $2z_g^*$. In this range, numerical focusing is possible, because no frequency is completely attenuated.

The optical sectioning effect with CCHM has been proved experimentally [3]. It was demonstrated that low spatial coherence of illumination allows for the effective suppression of images of seriously defocused objects in the in-focus image plane. This enables quantitative phase imaging of biological samples in turbid media, of thick specimen or in other diffuse environment.

4.2 Three-dimensional imaging

As mentioned above, the detailed theory of imaging with CCHM has been described [15] for all the possible configurations and illumination possibilities. The explanation of the basic statements can be found in [31]. Here, we only mention the transmitted light low coherent illumination case, since it is the setup configuration significant for the following parts.

4.2.1 Angular spectrum of a light wave

We start with a complex amplitude $u(\mathbf{q})$ of a monochromatic wave, which fulfils the Helmholtz equation. It can then be expressed by means of its angular spectrum $U(\mathbf{K}_t)$ as a superposition of plane waves

$$u(\mathbf{q}) = \iint_{-\infty}^{\infty} U(\mathbf{K}_t) \exp(2\pi i \mathbf{K} \cdot \mathbf{q}) d^2 \mathbf{K}_t, \quad (11)$$

where $\mathbf{q} = (\mathbf{q}_t, z) = (x, y, z)$ is a position vector in a three-dimensional Cartesian coordinate system and $\mathbf{K} = (\mathbf{K}_t, K_z) = (K_x, K_y, K_z)$ is a reduced wave vector. Both vectors are not normalised in this section. For the wave propagating in or against the direction of the axis z we define $K_z = \pm \sqrt{K^2 - K_t^2}$ respectively, with $K = |\mathbf{K}| = 1/\lambda = n/\lambda_v$ being a wave number, λ_v is the wavelength in vacuum, n is the refractive index of a medium and $K_t = |\mathbf{K}_t|$. We can then for the angular spectrum verify that it holds

$$U(\mathbf{K}_t) = \iint_{-\infty}^{\infty} u(\mathbf{q}) \exp(-2\pi i \mathbf{K} \cdot \mathbf{q}) d^2 \mathbf{q}_t. \quad (12)$$

The non-standard reduced wave vector \mathbf{K} is used here, because the theory is mostly derived in the space of spatial frequencies. The transverse components of \mathbf{K} then acquire the meaning of spatial frequencies. Evanescent waves are neglected.

4.2.2 Imaging by an optical system

The angular spectrum of a light wave gets transformed by the optical system of the microscope. We assume this transformation is stigmatic imaging within the isoplanatic region of the system. The wave is detected in the image plane. For notation simplification, the position of a point in the image plane is given by the coordinate vector \mathbf{q}_t of the optically conjugated point in the object plane. Let's then denote $u(\mathbf{q}_t)$ the complex amplitude in the object plane and $u'(\mathbf{q}_t)$ in the image plane. The two angular spectra, computed by eq. (11) are related by

$$U'(\mathbf{K}_t) = P_T(\mathbf{K}) U(\mathbf{K}_t), \quad (13)$$

where $P_T(\mathbf{K})$ describes the transfer of spatial frequencies by the imaging system. It is assumed to be a function for the whole vector \mathbf{K} , not just \mathbf{K}_t , to include also its dependence on wavelength. The waves propagate in the positive direction of the z axis, so $K_z = \sqrt{K^2 - K_t^2}$. It is evident that a plane wave is transformed into another plane wave. Because the coordinate system is common for both object and image plane, these two plane waves are specified by the same vector \mathbf{K} .

The function $P_T(\mathbf{K})$ is related to the 3D amplitude point spread function of the imaging system. Let's suppose imaging of a point object, for which $u(\mathbf{q}) = \delta(x)\delta(y)$. The corresponding angular spectra are then $U(\mathbf{K}_t) = 1$ and $U'(\mathbf{K}_t) = P_T(\mathbf{K})$ and are derived from eq. (12) and eq. (13). We substitute the last result into eq. (11) and derive the 3D distribution $p(\mathbf{q})$ of a complex amplitude round the Gaussian image point in the form of the inverse Fourier transform

$$p(\mathbf{q}) = \int\limits_{-\infty}^{\infty} \int\limits_{-\infty}^{\infty} P_T(\mathbf{K}) \exp(2\pi \mathbf{K} \cdot \mathbf{q}) d^2 \mathbf{K}_t. \quad (14)$$

This is why we also understand the function $P_T(\mathbf{K})$ as a 3D pupil function of the system. The formula for $P_T(\mathbf{K})$ can be derived but the details are not necessary for the following parts, therefore here we only mention its final form

$$P_T(\mathbf{K}) = \sqrt{\frac{K}{K_Z}} \text{circ}\left(\frac{K \cos \alpha}{K_Z}\right) = \sqrt{\frac{K}{K_Z}} \text{circ}\left(K_t \frac{\lambda_v}{\text{NA}}\right), \quad \text{circ}(x) = \begin{cases} 1 & \text{for } x < 1, \\ \frac{1}{2} & \text{for } x = 1, \\ 0 & \text{otherwise,} \end{cases} \quad (15)$$

which specifies the function $P_T(\mathbf{K})$ for a rotationally symmetrical aplanatic system. Again, NA denotes the numerical aperture of the imaging system, λ_v is the wavelength in vacuum and α is the angular aperture of the system in the object space. We suppose $K_Z \geq 0$ for the illumination wave. Let's also assume that the condenser is an aplanatic system characterized by angular aperture α_C and a pupil function $P_C(\mathbf{K})$ specified by eq. (15) with α substituted by α_C .

The support for $P_T(\mathbf{K})$ and $P_C(\mathbf{K})$ as defined above has the form of a cone with apex in the origin of a coordinate system in K -space, the cone aperture being α and α_C respectively and K_Z being the axis of the cone.

4.2.3 Illumination source

A generally broad and broadband source is used in CCHM. Each point of this source produces a parallel beam in the object spaces of both microscope arms. This applies to point with corresponding inclination of the beam lower than the angular aperture α_C of the condensers. The source is characterized by its spectral density. The condensers are assumed to fulfil the sine condition so the components K_x, K_y of the reduced wave vector of the beam are proportional to the Cartesian coordinates of the respective point of the source. The wave number K is determined by the assignment of all the coordinates K_x, K_y, K_z . For these reasons, we can define the spectral density of the source with function $i(\mathbf{K})$ of the vector \mathbf{K} .

The theory is derived firstly for fictitious monochromatic point source radiating with amplitude $\sqrt{i(\mathbf{K})}$ and a zero phase shift. According to the generalized Hopkins formula, the intensity $i(\mathbf{q}_t)$ for a real broad and broadband source is calculated by the integration of $i(\mathbf{q}_t; \mathbf{K})$ over the area and frequency range of the source, where $i(\mathbf{q}_t; \mathbf{K})$ is the intensity for the fictitious point source.. We already mentioned that the illumination fulfils the sine condition, and so the Jacobian determinant for the transformation of the coordinates and frequency of the source into the components of vector \mathbf{K} equals $K_z K^{-3}$ and a constant factor is omitted. We then have

$$i(\mathbf{q}_t) = \int \int \int_{-\infty}^{\infty} i(\mathbf{q}_t; \mathbf{K}) K_z K^{-3} d^3 \mathbf{K}. \quad (16)$$

We use the eq. (2) from Chap. 2.3 and substitute into eq. (16). Since the optical system of the microscope is assumed to be achromatic and spatially invariant, the phase modulation is independent of the integration variables. The reconstruction method used for separation of the signal term OR^* (eq. 2), Chap. 2.3) can be used for the separation of its integral, eq. (16), as well. The reconstructed holographic signal $w(\mathbf{q}_t)$ may then be expressed in the form

$$w(\mathbf{q}_t) = \int \int \int_{-\infty}^{\infty} O(\mathbf{q}_t; \mathbf{K}) R^*(\mathbf{q}_t; \mathbf{K}) K_z K^{-3} d^3 \mathbf{K}. \quad (17)$$

On substituting from the equations for coherent light source [15] into eq. (17), the integration over \mathbf{K} can be transformed into the integration over the scattering vector \mathbf{Q} . The expression for signal then simplifies to

$$w(\mathbf{q}_t) = \int \int \int_{-\infty}^{\infty} T(\mathbf{Q}) H(\mathbf{Q}) \exp(2\pi i \mathbf{Q} \cdot \mathbf{q}_t) d^3 \mathbf{Q}, \quad (18)$$

with $\mathbf{q}_t = (x, y, -z_s)$.

We have already seen this equation but for the two-dimensional case (eq. 4). The function $T(\mathbf{Q})$ denotes the 3D Fourier transform of the object scattering potential [15] and $H(\mathbf{Q})$ again denotes, in this case three-dimensional, coherent transfer function (CTF). We can express it as

$$H(\mathbf{Q}) = \int \int \int_{-\infty}^{\infty} i(\mathbf{K}) |P_C(\mathbf{K})|^2 P_T^*(\mathbf{K}) P_T(\mathbf{K} + \mathbf{Q}) C_R(\mathbf{K}) C_O(\mathbf{K}, \mathbf{Q}) \times \delta \left[K_Z + Z \mp \sqrt{K^2 - (\mathbf{K}_t^2 + \mathbf{Q}_t^2)} \right] K_Z K^{-3} d^3 \mathbf{K}, \quad (19)$$

where $C_O(\mathbf{K}, \mathbf{Q})$ and $C_R(\mathbf{K})$ are slowly varying correction functions or geometric factors in object and reference arm respectively (details may be found in [15]). The 3D CTF is describing completely the whole imaging process of CCHM, including the numerical reconstruction of a hologram.

4.2.4 Point spread function

The holographic signal $w(\mathbf{q}_i)$ is the product of $T(\mathbf{Q})$, the 3D Fourier transform of the scattering potential $t(\mathbf{q})$ of the object and of 3D CTF $H(\mathbf{Q})$. Therefore it can be also expressed as a 3D convolution

$$w(\mathbf{q}_i) = \int \int \int_{-\infty}^{\infty} t(\mathbf{q}) h(\mathbf{q} - \mathbf{q}_i) d^3 \mathbf{q} = t(\mathbf{q}_i) * h(\mathbf{q}_i), \quad (20)$$

where $h(\mathbf{q}_i)$ is a three-dimensional point spread function (PSF), which is the Fourier transform of 3D CTF,

$$h(\mathbf{q}_i) = \int \int \int_{-\infty}^{\infty} H(\mathbf{Q}) \exp(2\pi i \mathbf{Q} \cdot \mathbf{q}_i) d^3 \mathbf{Q}. \quad (21)$$

Obviously, the imaging process is always coherent, no matter what the coherence properties of the illumination are. These properties only determine the behaviour of $H(\mathbf{Q})$ and the shape of its support, which coincides with the range of spatial frequencies transferred by the microscope.

4.2.5 The three-dimensional coherent transfer function

Defining the imaging by a system by its CTF is practical, since we can easily compare the transfer of spatial frequencies by comparing the CTF for arbitrary degree of coherence of the illumination. The dependence of CTF on coherence properties is illustrated in fig. 6, but on a modified function $H(\mathbf{Q}) \cdot \mathbf{Q}$, which keeps the passband of the CTF but eliminates the singularity in the origin of the coordinate system.

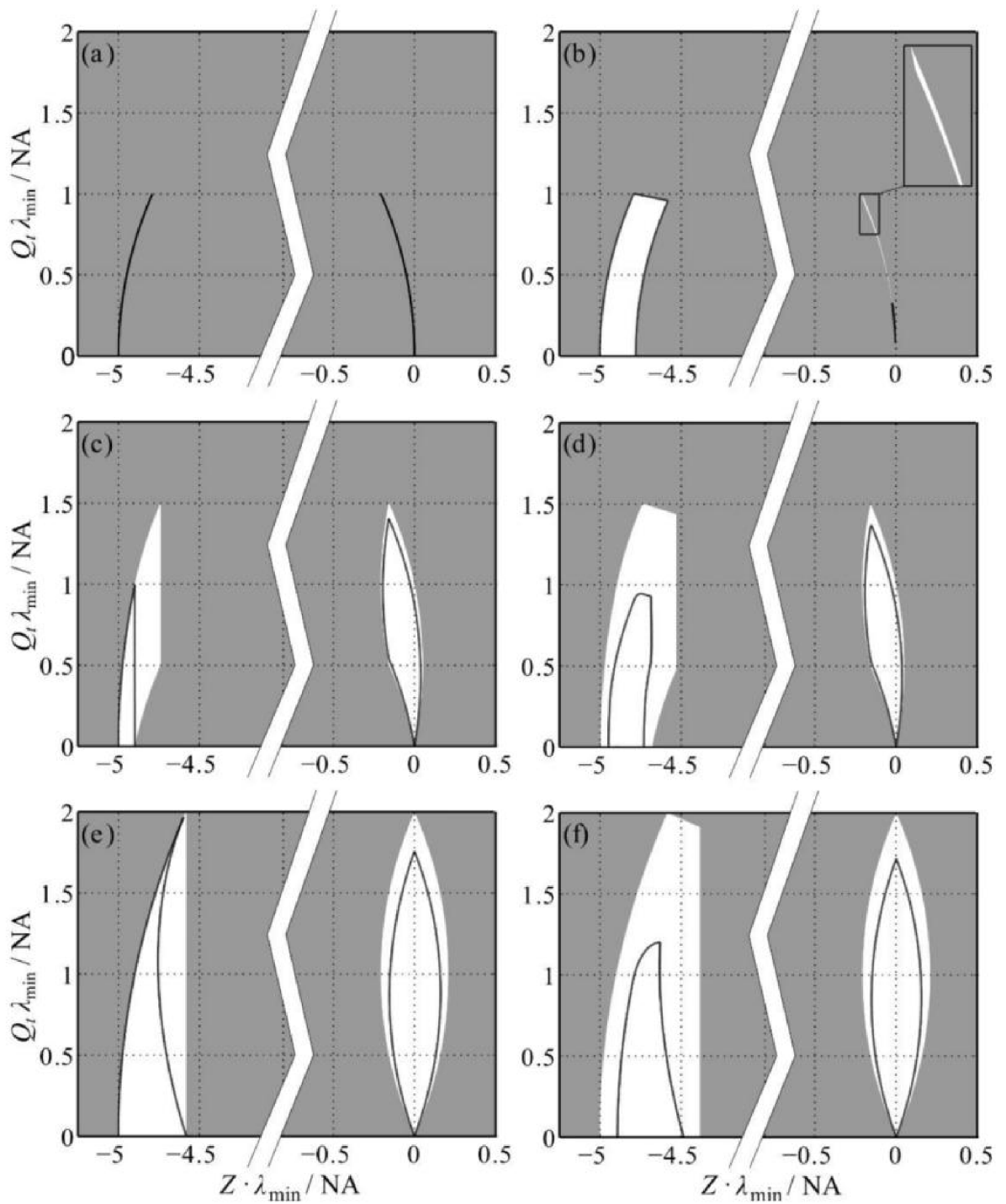


Figure 6: Cross sections of rotationally symmetrical function $H(\mathbf{Q}) \cdot \mathbf{Q}$, representing the 3D CTF: left part of each graph represents the reflected light, right side represents the transmitted light situation; (a), (c), (e) monochromatic source; (b), (d), (f) spectrally broad source; (a), (b) point source; (c), (d) broad source, $NA_S = NA/2$; (e), (f) broad source, $NA_S = NA$; The support of the function is shown as the white area, the solid black line represents the half-maximum value of $H(\mathbf{Q}) \cdot \mathbf{Q}$ [15].

Let's emphasise some of the imaging properties that can be deduced from the behaviour of the 3D CTF. Some of them were already mentioned in Chap. 3 but not as a result of the CTF shape and support.

Firstly, wider passband in some direction corresponds to a better resolution in the same direction. Fig. 6 shows that the highest lateral resolving power corresponds to the highest possible aperture of illumination, $NA_S = NA$ (fig. 6 (e), (f)), and so to the lowest possible spatial coherence of illumination.

More importantly for the aim of this thesis, the longitudinal resolving power is related to localizing any axially narrow structure. The wider is the passband axially for a defined transverse frequency, the better is the localization of this particular structure, which has this transverse frequency, in the axial direction. In the wide sense, this is how the optical section is created. With coherent illumination, only one transverse frequency is transferred and therefore no axial structure can be localized. In the transmitted-light arrangement, increasing the illumination numerical aperture NA_S , and so lowering the spatial coherence, induces the coherence gating effect and optical sectioning. However, this effect arises for non-zero transverse frequencies only.

5 Simulations

The very first simulations of the phase distribution of imaged living cell model [3] were calculated numerically using the Rytov approximation. They simulate CCHM imaging according to the theory explained in Chap. 3 derived from [15] and they show a trend of better axial localization for higher numerical aperture NA_S . This gave an impulse for further research and it was also the initial motivation for this thesis.

For proving the relationship between the spatial coherence (i. e. NA_S) and axial localization, a reference sample was needed, which could be not only simulated on the same principle but also prepared and measured with CCHM. This chapter introduces the theory of scattering from inhomogeneous media, especially the Rytov approximation [31]. The theory, which is necessary for the simulations is followed by the simulations of the reference sample CCHM imaging and also by the description of the sample preparation, which was for crucial for the experimental part.

5.1 Scattering from inhomogeneous media

All theory is derived from [31] where more details and further explanation can be found. In order to derive the basic integral equation in the scalar theory of scattering, we consider a monochromatic electromagnetic field with time dependence $\exp(-i\omega t)$ incident on a linear isotropic medium occupying a finite domain V (fig. 7). We also assume that no sources are present in V . Then the space-dependent part of the complex electric field will satisfy the equation, specialized only to a monochromatic field:

$$\nabla^2 \mathbf{E}(\mathbf{r}, \omega) + k^2 \varepsilon(\mathbf{r}, \omega) \mathbf{E}(\mathbf{r}, \omega) + \text{grad}[\mathbf{E}(\mathbf{r}, \omega) \cdot \text{grad} \ln \varepsilon(\mathbf{r}, \omega)] = 0, \quad (22)$$

where

$$k = \frac{\omega}{c}. \quad (23)$$

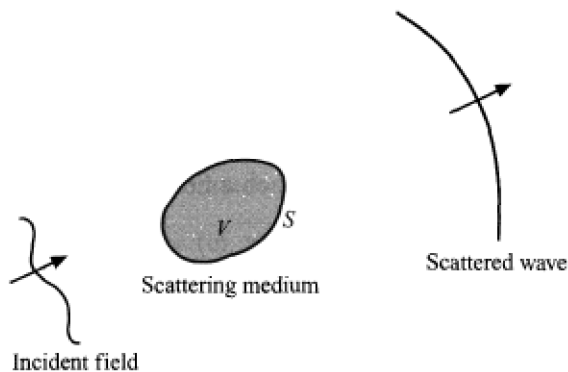


Figure 7: Illustration of a general scattering situation. Scattering medium is occupying a volume V , bounded by a closed surface S [31].

Because the last term on the left side of eq. (22) couples the Cartesian components of the electric field, the treatment of scattering based on this equation is rather complicated. To simplify it, we assume dielectric 'constant' $\varepsilon(\mathbf{r})$ that varies very slowly with position so it is effectively constant over distances close to the wavelength $\lambda = 2\pi/k = 2\pi c/\omega$. Therefore we can neglect the term from eq. (22) and obtain the equation

$$\nabla^2 \mathbf{E}(\mathbf{r}, \omega) + k^2 n^2(\mathbf{r}, \omega) \mathbf{E}(\mathbf{r}, \omega) = 0, \quad (24)$$

using the Maxwell formula $\varepsilon(\mathbf{r}, \omega) = n^2(\mathbf{r}, \omega)$, where $n(\mathbf{r}, \omega)$ stands for the refractive index of the medium. The Cartesian components of $\mathbf{E}(\mathbf{r}, \omega)$ are not coupled anymore, which makes eq. (24) easier to analyse in comparison with eq. (22). A good insight into the general behaviour of the scattered field can be obtained by studying the solution of eq. (24) for a single Cartesian component of $\mathbf{E}(\mathbf{r}, \omega)$. We denote the component $U(\mathbf{r}, \omega)$ and rewrite eq. (24) into following scalar equation, which will be a starting point for scattered field analysis:

$$\nabla^2 U(\mathbf{r}, \omega) + k^2 n^2(\mathbf{r}, \omega) U(\mathbf{r}, \omega) = 0. \quad (25)$$

It is practical to rewrite eq. (25) in the form

$$\nabla^2 U(\mathbf{r}, \omega) + k^2 U(\mathbf{r}, \omega) = -4\pi F(\mathbf{r}, \omega) U(\mathbf{r}, \omega), \quad (26)$$

with

$$F(\mathbf{r}, \omega) = \frac{1}{4\pi} k^2 [n^2(\mathbf{r}, \omega) - 1]. \quad (27)$$

The function $F(\mathbf{r}, \omega)$ is called *the scattering potential* of the medium.

Let's now express $U(\mathbf{r}, \omega)$ as the sum of the incident field and the scattered field:

$$U(\mathbf{r}, \omega) = U^{(i)}(\mathbf{r}, \omega) + U^{(s)}(\mathbf{r}, \omega). \quad (28)$$

The incident field is usually a plane wave. Such a field satisfies the Helmholtz equation

$$(\nabla^2 + k^2) U^{(i)}(\mathbf{r}, \omega) = 0 \quad (29)$$

through the whole space. Using substitution, combining the described equations and using Green's function (these steps are not necessary to be showed here and can be found in [31]) we obtain the following relation

$$U^{(s)}(\mathbf{r}, \omega) = \int_V F(\mathbf{r}', \omega) U(\mathbf{r}', \omega) \frac{e^{ik|\mathbf{r}-\mathbf{r}'|}}{|\mathbf{r}-\mathbf{r}'|} d^3r \quad (30)$$

for the scattered field, which we assume behaves as an outgoing spherical wave far away from the scatterer. Suppose the incident field is a monochromatic plane wave of unit amplitude and frequency ω , propagating in the direction specified by real unit vector \mathbf{s}_0 . The time independent part of the incident wave is given by the expression

$$U^{(i)}(\mathbf{r}, \omega) = e^{ik\mathbf{s}_0 \cdot \mathbf{r}} \quad (31)$$

and so we see from eq. (30) and eq. (31) that

$$U(\mathbf{r}, \omega) = e^{iks_0 \cdot \mathbf{r}} + \int_V F(\mathbf{r}, \omega) U(\mathbf{r}, \omega) \frac{e^{ik|\mathbf{r}-\mathbf{r}'|}}{|\mathbf{r}-\mathbf{r}'|} d^3r. \quad (32)$$

Eq. (32) is called the *integral equation of potential scattering* and it is the basic equation for determining $U(\mathbf{r}, \omega)$. However, it is only an integral equation for $U(\mathbf{r}, \omega)$ at points within the scattering volume V . Once the solution inside V is known, the solution in the exterior point can be obtained by substituting the solution to the interior problem in the integrand of eq. (32).

5.1.1 The first-order Born approximation

In most practical applications it is impossible to solve the integral equation of potential scattering (eq. 32) in a closed form. Therefore it needs to be solved by some approximate technique. Usually, for weakly scattering medium, a perturbation method is used, in which the successive terms in the perturbation expansion are found by iteration from the previous ones. The lowest order approximation provides a rough insight into various features of scattering. We say that a medium is weakly scattering if its refractive index differs only slightly from unity. Due to that, we assume that a good approximation of the total field U can be obtained if the term $U = U^{(i)} + U^{(s)}$ in the integral in eq. (32) is replaced by $U^{(i)}$ only. The expression

$$U(\mathbf{r}) \sim U_1(\mathbf{r}) \equiv e^{iks_0 \cdot \mathbf{r}} + \int_V F(\mathbf{r}') e^{iks_0 \cdot \mathbf{r}'} \frac{e^{ik|\mathbf{r}-\mathbf{r}'|}}{|\mathbf{r}-\mathbf{r}'|} d^3r' \quad (33)$$

is the first approximation to the solution of the integral equation of scattering (from now, the dependence on the frequency ω is not displayed). This approximate solution is referred to as the Born approximation, more precisely the *first-order Born approximation*.

From the consequences of this approximation we only mention two. Firstly, there is the problem of inverse scattering, i. e. the problem of obtaining information about an object from measurement of the field scattered by it. Another very important drawback is the resolution limit. It cannot be clearly stated but the approximation contains information about details with resolution limit about the order of the wavelength. Therefore, the resolution on high spatial frequencies is limited.

Using the method of perturbation, higher order Born approximations are obtained and multiple scattering can be described.

5.1.2 The Rytov approximation

Instead of representing the solution of eq. (32) as a perturbation series, a different expansion may be used, according to Rytov [34]. The Rytov expansion is often used in diffraction tomography and wave propagation in random media. We start from eq. (26) with the scattering potential from eq. (27). The refractive index is noted $n(\mathbf{r})$. The important difference of the Rytov procedure is expressing $U(\mathbf{r}, \omega)$ as

$$U(\mathbf{r}, \omega) = e^{\psi(\mathbf{r}, \omega)}, \quad (34)$$

where ψ is generally complex and is then expanded rather than U in perturbation series.

We now put $A(\mathbf{r}, \omega)$ as the amplitude and $\phi(\mathbf{r}, \omega)$ as the real phase of $U(\mathbf{r}, \omega)$, so

$$U(\mathbf{r}, \omega) = A(\mathbf{r}, \omega)e^{i\phi(\mathbf{r}, \omega)}. \quad (35)$$

It is then evident that

$$\psi(\mathbf{r}, \omega) = \ln A(\mathbf{r}, \omega) + i\phi(\mathbf{r}, \omega). \quad (36)$$

We substitute from eq. (34) into eq. (26) and obtain the following equation for ψ :

$$\nabla^2 \psi(\mathbf{r}, \omega) + [\nabla \psi(\mathbf{r}, \omega)]^2 = -k^2 n^2(\mathbf{r}, \omega). \quad (37)$$

This is a nonlinear equation which has the mathematical form of the so-called Riccati equation.

We again assume the refractive index $n(\mathbf{r}, \omega)$ to differ only slightly from unity so that

$$n(\mathbf{r}, \omega) = 1 + \delta n(\mathbf{r}, \omega), \quad (\delta n \ll 1). \quad (38)$$

For convenience, we introduce a perturbation parameter μ which will be keeping track of the powers of various terms in the perturbation parameters. We put

$$\delta n(\mathbf{r}) = \frac{1}{2} \mu \beta(\mathbf{r}). \quad (39)$$

It then follows that

$$n^2 \approx 1 + 2\delta n = 1 + \mu \beta, \quad (40)$$

and so eq. (37) becomes

$$\nabla^2 \psi(\mathbf{r}, \omega) + [\nabla \psi(\mathbf{r}, \omega)]^2 + k^2 + k^2 \mu \beta(\mathbf{r}) = 0. \quad (41)$$

Using the expansion known as Liouville-Neumann series, this may be expressed in the form

$$U(\mathbf{r}) = U^{(0)}(\mathbf{r}) + U^{(1)}(\mathbf{r}) + U^{(2)}(\mathbf{r}) + \dots, \quad (42)$$

where $U^{(0)} \equiv U^{(i)}$ denotes the incident field, assuming it is a homogenous plane wave or a linear superposition of such waves. $U^{(1)} \equiv U_1 - U_0$ is linear in the scattering potential $F(\mathbf{r})$, $U^{(2)} \equiv U_2 - U_1$ is quadratic in the scattering potential, etc. In the Rytov method, one expands the $\psi(\mathbf{r})$ in a similar way, as already mentioned above:

$$\psi(\mathbf{r}) = \psi_0(\mathbf{r}) + \mu \psi_1(\mathbf{r}) + \mu^2 \psi_2(\mathbf{r}) + \dots, \quad (43)$$

where ψ_1 is linear in F , ψ_2 is quadratic, etc. Eq. (35) for the total field then becomes

$$U(\mathbf{r}) = e^{[\psi_0(\mathbf{r}) + \mu\psi_1(\mathbf{r}) + \mu^2\psi_2(\mathbf{r}) + \dots]}, \quad (44)$$

which is known as the *Rytov expansion*.

By substituting the expansion from eq. (43) into the Riccati equation (eq. 37) and equating the groups of terms containing equal powers of the perturbation parameter μ , one can obtain recurrence relations for the successive terms and find that

$$(\nabla^2\psi_0) + (\nabla\psi_0)^2 = -k^2, \quad (45)$$

$$\nabla^2\psi_1 + 2\nabla\psi_0 \cdot \nabla\psi_1 = -k^2\beta, \quad (46)$$

$$\nabla^2\psi_2 + 2\nabla\psi_0 \cdot \nabla\psi_2 = (\nabla\psi_1)^2, \quad (47)$$

$$\nabla^2\psi_3 + 2\nabla\psi_0 \cdot \nabla\psi_3 = -2(\nabla\psi_1) \cdot (\nabla\psi_2), \quad (48)$$

$$\vdots \quad \quad \quad \vdots \quad \quad \quad \vdots \quad \quad \quad \vdots \quad \quad \quad \vdots$$

$$\nabla^2\psi_n + 2\nabla\psi_0 \cdot \nabla\psi_n = -\sum_{k=1}^{n-1} \nabla\psi_n \cdot \nabla\psi_{n-k}. \quad (49)$$

The first equation of this expansion, eq. (45), is independent of the medium and therefore ψ_0 must be associated with the incident field $U^{(i)}$,

$$e^{\psi_0(\mathbf{r},\omega)} = U^{(i)}(\mathbf{r},\omega). \quad (50)$$

All the other equations, eq. (46 - 49), are in the form

$$\nabla^2\psi_n + 2\nabla\psi_0 \cdot \nabla\psi_n = -g_n. \quad (51)$$

The factor g_n is known, if all the preceding equations have been solved. Eq. (51) can be reduced to a known form, using the substitution

$$\psi_n(\mathbf{r},\omega) = e^{-\psi_0(\mathbf{r},\omega)} W_n(\mathbf{r},\omega) \quad (52)$$

Now, if we calculate $\nabla\psi_n$ and $\nabla^2\psi_n$, and using eq. (45), we reduce eq. (51) to

$$\nabla^2 W_n + k^2 W_n = -g_n e^{\psi_0}. \quad (53)$$

In eq. (53) we recognize the inhomogeneous Helmholtz equation for W_n . It may be solved in similar way as eq. (30 - 32) was obtained from eq. (29), when the right side of eq. (53) is known. The requirement on W_n to behave as an outgoing spherical wave at infinity is then given by integral

$$W_n(\mathbf{r},\omega) = \frac{1}{4\pi} \int_V g_n(\mathbf{r}',\omega) U(\mathbf{r},\omega) e^{\psi_0(\mathbf{r}',\omega)} \frac{e^{ik|\mathbf{r}-\mathbf{r}'|}}{|\mathbf{r}-\mathbf{r}'|} d^3r'. \quad (54)$$

Finally, from eq. (52) and eq. (54), we obtain the expression for ψ_n

$$\psi_n(\mathbf{r},\omega) = \frac{1}{4\pi} e^{-\psi_0(\mathbf{r},\omega)} \int_V g_n(\mathbf{r}',\omega) U(\mathbf{r},\omega) e^{\psi_0(\mathbf{r}',\omega)} \frac{e^{ik|\mathbf{r}-\mathbf{r}'|}}{|\mathbf{r}-\mathbf{r}'|} d^3r'. \quad (55)$$

Now, returning to the Rytov expansion, eq. (44), but using only the first two components in the exponent we get

$$U(\mathbf{r}, \omega) \approx U_1^{(R)}(\mathbf{r}, \omega) = e^{\psi_0(\mathbf{r}, \omega) + \psi_1(\mathbf{r}, \omega)}. \quad (56)$$

$U_1^{(R)}$ is called the Rytov approximation, or better the *first-order Rytov approximation*.

To demonstrate the relation between the first-order Born approximation and the first-order Rytov approximation, we use eq. (50) and see that

$$U_1^{(R)}(\mathbf{r}, \omega) = U^{(i)}(\mathbf{r}, \omega) e^{\psi_1(\mathbf{r}, \omega)}, \quad (57)$$

and we note that ψ_1 can be expressed in a simple way through the first Born approximation (detailed explanation again found in [31]). The relation between the two approximations is expressed in equation

$$\psi_1(\mathbf{r}, \omega) = [U^{(i)}(\mathbf{r}, \omega)]^{-1} [U_1^{(s)}(\mathbf{r}, \omega)]^{(B)} \quad (58)$$

where $[U_1^{(s)}]^{(B)}$ represents the scattered field in the first-order Born approximation with an arbitrary field $U^{(i)}(\mathbf{r}, \omega)$ incident on the scatterer:

$$[U_1^{(s)}]^{(B)} = \frac{k^2}{4\pi} \int_V [n^2(\mathbf{r}', \omega) - 1] U^{(i)}(\mathbf{r}', \omega) \frac{e^{ik|\mathbf{r}-\mathbf{r}'|}}{|\mathbf{r}-\mathbf{r}'|} d^3r. \quad (59)$$

There is no clear consensus whether one or the other approximation is better and the topic has been discussed in many publications. The simulations of living cell model [3] showed more accurate results for the first-order Rytov approximation, therefore it has also been used for the simulations in this thesis.

5.2 Theoretical simulation

To obtain a rough idea of the axial localization, we theoretically simulated a structure, similar to the one we expected to use as a reference sample, weakly resembling a cell with its organelles. This sample was later manufactured and the simulation parameters adjusted, as described further in this chapter. Here we illustrate the numerical calculation based on the theory of three-dimensional imaging [15] and scattering described by the Rytov approximation [31]. The MATLAB simulations depicted in this chapter are a courtesy of prof. RNDr. Jiří Petráček, Dr.

We simulated the scattering from an object using the 1st Rytov approximation and calculated numerically the scattering matrix $\mathcal{S}(\mathbf{K}'_t, \mathbf{K}_t)$ of our reference sample. Here, \mathbf{K}'_t , \mathbf{K}_t are lateral coordinates of the reduced wave vector \mathbf{K}' , \mathbf{K} of a primary plane wave and of a plane-wave component of the scattered wave respectively. The magnitude of the reduced wave vectors is $1/\lambda_v$, where λ_v is a wavelength of the quasi-monochromatic illumination in vacuum. The scattering matrix is used in the formula for the image signal of CCHM, derived in [15]. The holographic signal is expressed as

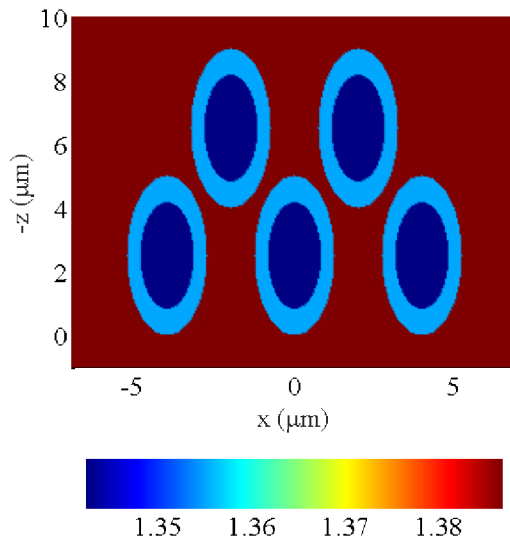


Figure 8: Model of a reference object used for a MATLAB simulation.

$$\begin{aligned}
 w(\mathbf{q}_t) = & \iint_{-\infty}^{\infty} \iint_{-\infty}^{\infty} \mathcal{S}(\mathbf{K}'_t, \mathbf{K}_t) \times \\
 & \times \text{circ}\left(\frac{\lambda_v}{\text{NA}_S} \mathbf{K}_t\right) \text{circ}\left(\frac{\lambda_v}{\text{NA}} \mathbf{K}'_t\right) \exp[i2\pi(\mathbf{K}'_t - \mathbf{K}_t) \cdot \mathbf{q}_t] d^2\mathbf{K}'_t d^2\mathbf{K}_t,
 \end{aligned} \tag{60}$$

where the circ functions are used for the approximation of the transfer functions.

We planned to prepare the sample as a three-dimensional structure of five ellipsoids [35]. The ellipsoid elements are the size of $2.5 \mu\text{m} \times 5 \mu\text{m}$ and the refractive index in their centre is smaller by 0.04 compared to the surrounding environment. The refractive index changes gradually, rather than by step, and this is simulated by creating a “core” with a refractive index in between the center of the element and the surroundings. The distance between the elements in one row is $4 \mu\text{m}$ and the upper row is $4 \mu\text{m}$ above the bottom one. The structure, modelled by the 3D refractive index distribution, is shown in fig. 8.

If we now simulate the three-dimensional imaging of the refractive index difference with holographic microscope, we acquire a xz cross section of its phase distribution (fig. 9). The important parameters that influence the results are NA, the numerical aperture of the objectives, and the wavelength λ . Assuming the experiment to be done with $20\times$ magnification objectives, NA is 0.5 and the wavelength used in CCHM is $\lambda = 650 \text{ nm}$. The simulation is then run for various NA_S , the illumination numerical aperture, in other words for various spatial coherence.

In fig. 9, from left to right, the numerical aperture NA_S of the illumination increases and at the same time the spatial coherence decreases. With lower NA_S of the condensers,

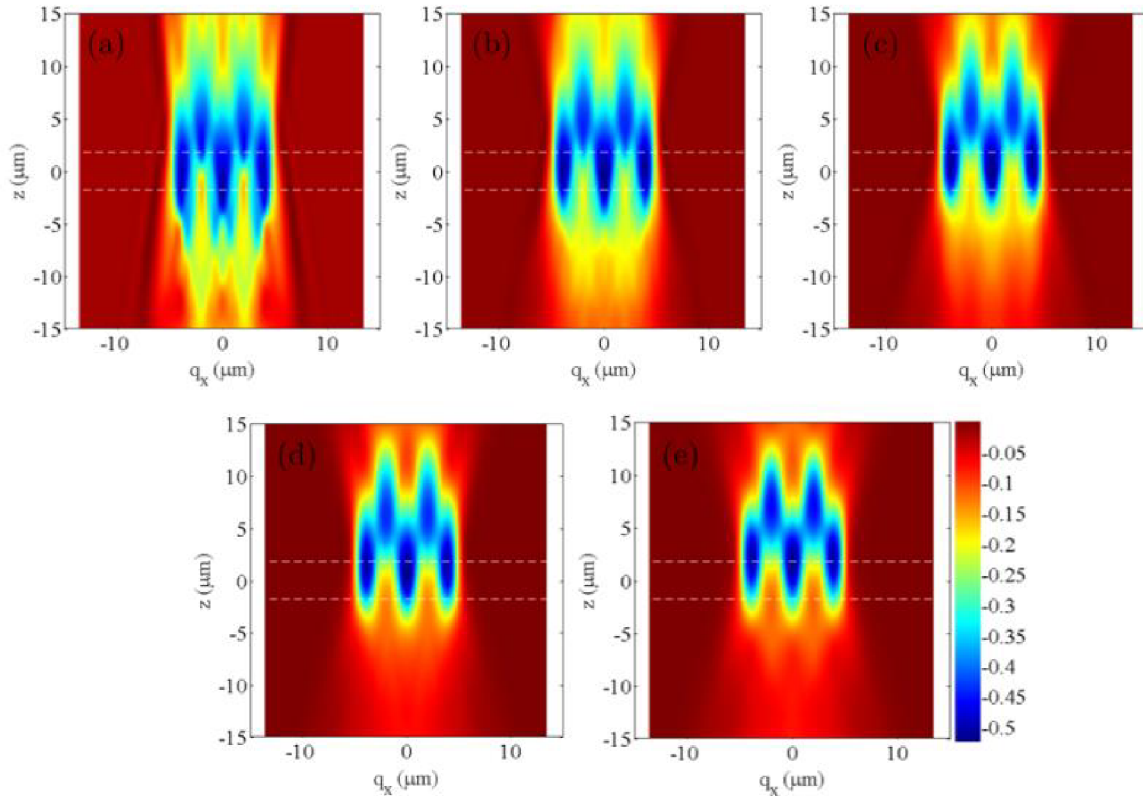


Figure 9: Simulation of xz cross section of a phase distribution for $\text{NA} = 0.5$, $\lambda = 650 \text{ nm}$; (a) $\text{NA}_S = 0.1$, (b) $\text{NA}_S = 0.2$, (c) $\text{NA}_S = 0.3$, (d) $\text{NA}_S = 0.4$, (e) $\text{NA}_S = 0.5$.

when closing the aperture, we also lower the diameter of the effective area of the light source and so we create a spatially coherent source. If the aperture is maximally open, i. e. the aperture of the objective is fully filled by the image of the source, we create a light source that is completely spatially incoherent [13].

Let's now take a look at fig. 9. We can clearly state, as expected according to [3], that there is a trend of improvement in axial localization with increasing NA_S , i. e. lower degree of spatial coherence. The left most image suffers significantly from the issues of coherent imaging and we see a “ghost” shadow above and below the actual image of the structure. On the other hand, for the case on incoherent illumination, the axial localization seems quite precise. The axial length of one structure element, as we can estimate it visually in the image, for incoherent illumination is roughly $8 - 10 \mu\text{m}$, so $1 - 1.5 \times$ the real length, which defines the best value achievable experimentally. This trend should be obvious also in real microscope observation and so it became the main task for the experimental measurement.

Obviously this trend should go even further and one can expect the image to be even more degraded for extremely coherent illumination and also better axially resolved for incoherent illumination and higher NA. To demonstrate that, we simulated an extreme case for $\text{NA} = 0.95$, which unfortunately could not be verified by experiment because

such objectives do not have the working distance necessary for imaging a thick (three-dimensional) sample. Nevertheless, in fig. 10, we can compare the simulation results for the extreme cases. The middle one, for $\text{NA}_S = 0.3$ is fully comparable to the partially coherent cases of fig. 9. In the coherent situation (a), the imaged structure almost disappears in the “ghost” shadows, while in the completely incoherent case (c), the phase distribution resembles strongly the refractive index distribution of our simulated object. Although, in the area between the upper and bottom row of the structure elements, a connection among the elements appears that would be rather improbable in real microscopic three-dimensional imaging.

The trend of increasing axial localization was crucial for interpreting the experiment, although the simulation parameters needed to be adjusted to better describe the structures manufactured in the sample.

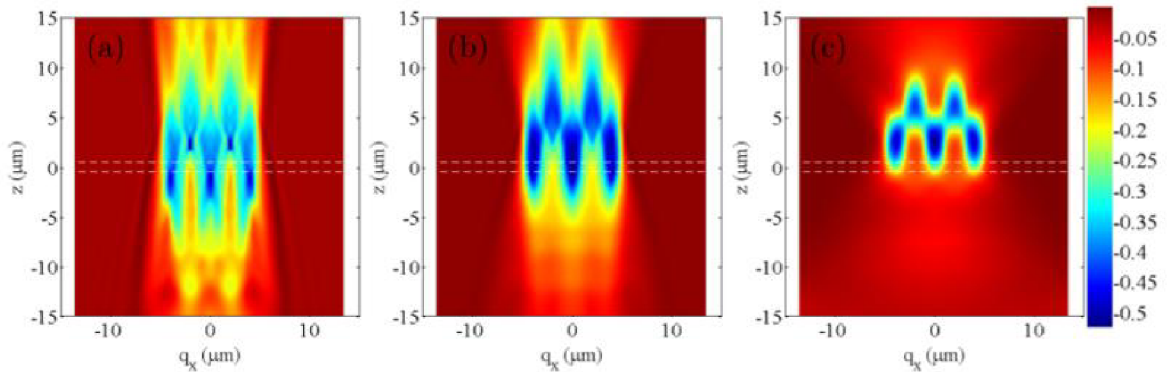


Figure 10: Simulation of xz cross section of phase distribution for extreme illumination conditions, $\text{NA} = 0.95$, $\lambda = 650 \text{ nm}$; (a) $\text{NA}_S = 0.1$, (b) $\text{NA}_S = 0.3$, (c) $\text{NA}_S = 0.95$.

5.3 Sample preparation

The sample for experimental verification of the simulations was chosen to be prepared by modification of a hydrogel. The hydrogel sample KVR58-G10-PP, $800 \mu\text{m}$ thick, a material based on hydroxyethylmetakrylate (HEMA) was cut into a thin strip. It has been shown that this material can be modified by a two-photon microscope and that the modified areas have lower refractive index than the original material [35,36]. The refractive index n of this particular material is not precisely defined, since the material properties depend on the absorption of water. The value of n given by the material provider is 1.3939 ± 0.0034 . For our purpose it is sufficient to know that there is a refractive index difference between the modified area and its surroundings.

The modifications were performed in regime LineScan by Femto2D-Galvo (Femtonics) microscope using Ti - sapphire femtosecond laser Coherent Chameleon Ultra II on the wavelength $\lambda = 700 \text{ nm}$. The beam was focused by objective Olympus $20 \times / \text{NA} = 0.5$ approximately $400 \mu\text{m}$ under the surface of the hydrogel, so about the middle of the strip.

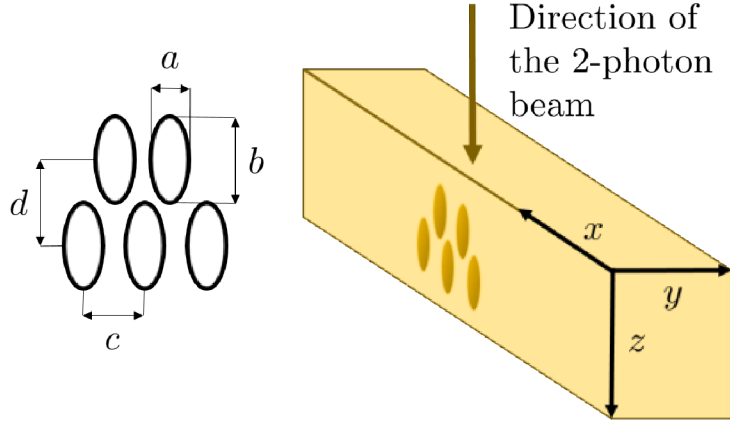


Figure 11: Schema of hydrogel modification and important parameters of the modified structures.

The hydrogel strip was placed in a chamber $800\ \mu\text{m}$ high, where it was kept between two cover slips in PBS solution (Phosphate Buffered Saline). The modifications were carried out as close to the edge of the strip as possible, to enable imaging the structures with CCHM also from the side, not only as a z -stack. Because the edge of the hydrogel strip was not straight, but rather rough, the modification was performed around $60 - 80\ \mu\text{m}$ from the edge. For better understanding of the sample preparation process, see right side of fig. 11. The modification is done in one point but it in fact creates an ellipsoid area, which is cylindrically symmetrical. It would be convenient, for proper axial localization examination, to place the elements directly in line above each other. Unfortunately, this was not achievable with the technique used, since the point modification became unpredictably prolonged in z direction.

The hydrogel material has a consistence best comparable to a dense jelly. The manipulation with a small piece of it, as our strip was, was difficult and the sample was fragile when taken with tweezers. Therefore it was handled carefully and taken only using special plastic tweezers, used for contact lenses, which are made of similar material. Due to the mechanical instability of the material, the strip could not be cut precisely and the edges were rough. Although the strip was placed in the chamber of the same height as was the thickness of the hydrogel ($800\ \mu\text{m}$), the sample was floating in PBS and it was likely to move, both during the modification and later during the microscope observation with CCHM. Due to that, it did not serve as such a good reference as expected, but even though it was useful for acquiring some results.

The size of structure elements was quite unpredictable, therefore the side (xz) view of the actual prepared sample was necessary. From that, the real dimensions of the elements, labelled a and b in fig. 11 were measured and the average value taken as a default one for the next simulation. The laser intensity while performing the modifications was 50 % of its maximum but the source was not completely stable so its performance may differ.

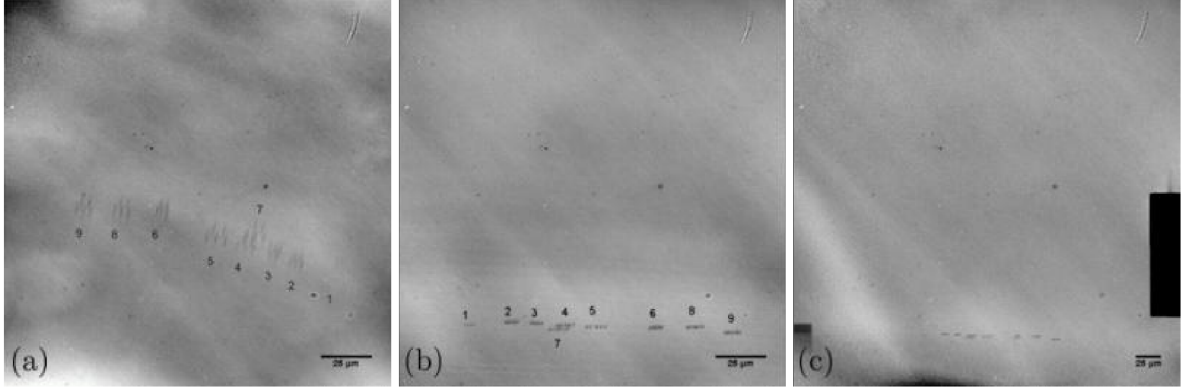


Figure 12: Modified structures in hydrogel, CCHM, compensated phase: (a) view in xz plane, (b) view in xy plane, (objectives $20 \times /0.5$) (c) mutual position with square marks for easier localization of the structures (objectives $10 \times /0.3$).

The phase image of the final version of the sample that was manufactured is in fig. 12, where (a) is the xz side view and (b) is the xy view in the direction of the modifying beam. The total amount of nine structures was created in the hydrogel strip. Except #1, they were all modified with 50 % of the laser intensity, for #1 it was only 40 % and therefore it is almost invisible. The structures differ in parameters c and d from fig. 11, i. e. the distance between the elements of the structure and the upper and the bottom row of them. Also, all the structures were not placed in the the same Z position (same depth bellow the hydrogel surface). The parameters of the structures are listed in tab. 1. The dimensions of the structure elements, which we used for the adjusted simulation, were $a = 2.2 \mu\text{m}$ and $b = 7.0 \mu\text{m}$. Because of the very low phase difference and small size of the structure array, it would be later difficult to find it with CCHM. Therefore, two square marks were modified in the hydrogel on both ends of the array, to make the future localization of the structures possible (fig. 12 (c)).

Structure	#1	#2	#3	#4	#5	#6	#7	#8	#9
c/d ($\mu\text{m}/\mu\text{m}$)	3/3	3/3	3/3	4/4	5/5	3/4	4/5	4/5	4/4
Depth (μm)	400	400	397	400	400	395	395	400	400

Table 1: Parameters of the structures modified in hydrogel.

5.4 Simulation of the prepared hydrogel sample

As we mentioned before, the theoretical simulation was done with the following parameters: $a = 2.5 \mu\text{m}$, $b = 5.0 \mu\text{m}$, $c = d = 4.0 \mu\text{m}$. But after the observation and measurement of the sample, they had to be adjusted to: $a = 2.2 \mu\text{m}$, $b = 7.0 \mu\text{m}$, $c = d = 5.0 \mu\text{m}$. Although the modified structures had various parameters c and d , the simulation was done only for the parameters of the structure #5, because we chose it as the best reference. All the other structures were hardly resolved. These results are discussed in Chap. 6.

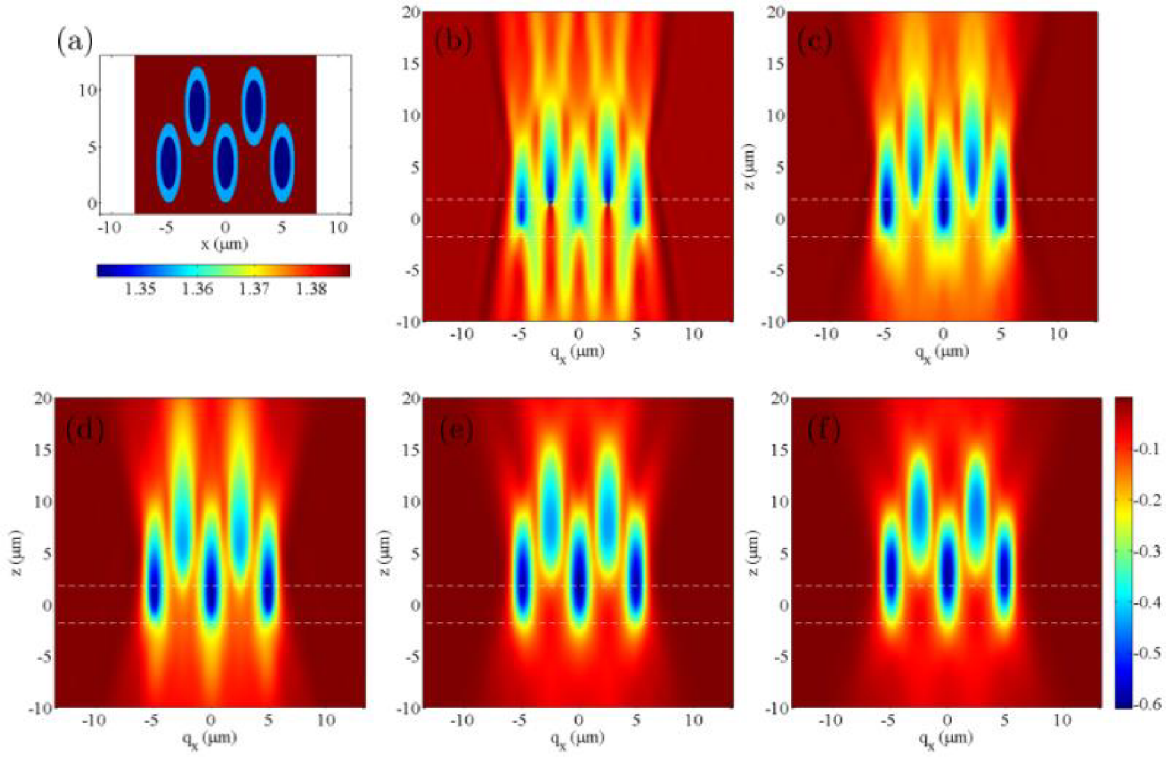


Figure 13: (a) Model of a modified structure #5; Simulation of xz cross section of phase distribution for $\text{NA} = 0.5$, $\lambda = 650$ nm; (b) $\text{NA}_S = 0.1$, (c) $\text{NA}_S = 0.2$, (d) $\text{NA}_S = 0.3$, (e) $\text{NA}_S = 0.4$, (f) $\text{NA}_S = 0.5$.

The results of the simulation of structure #5 are in fig. 13. Obviously the resolution as well as the axial localization should be better in comparison with the theoretical simulation, fig. 9. This is caused by the rather wide spacing between the elements of the structure. In (b) and (c) of fig. 13, the case of high degree of coherence of the illumination, we can see that the “ghost” shadow is still destroying the whole image. Even though the structure seems very well-resolvable, the phase difference between the centre of each element and its surroundings is very low. Especially in the y direction, the phase fades away gradually and quite slowly. In the case of incoherent illumination, (fig. 13 (f)), the shape of the structure is nicely preserved. The axial length of one element is about $10 - 14 \mu\text{m}$, depending on the phase difference we chose as a limit, so again roughly $1.5\times$ the real length.

6 Experiments and results

The experimental work had three very different parts. Firstly, there was the sample preparation. The sample was necessary for the experimental verification of the theory and the simulations (Chap. 5) and therefore was of particular importance. The process of its preparation is described mainly in section 5.3. Second significant task was the adaptation of the microscope setup for the use of condenser optics with high numerical aperture and low optical aberrations. This was also one of the goals of this thesis. Naturally, most important was the actual measurement of the sample and comparison of the images acquired with the original microscope setup and after the realization of the system adaptation and also with the simulation. The results and the process of their acquisition is presented in this chapter. All the measurements were carried out with light source bandpass filter $\lambda = 650 \text{ nm}$, 10 nm FWHM and the $20 \times /0.5$ objectives were used for imaging.

Most of the data sets are z-stacks, automatically taken via a build-in software function. For each stack, the position with best focus of all the structure elements was found. Then, the z-stack was acquired in the range $\pm 12 \mu\text{m}$ with $0.1 \mu\text{m}$ step. This way, 241 images in different planes of the sample were taken in each z-stack. These stacks were then viewed in their xz cross sections and the image of the chosen structure was cropped out. All data has been processed using ImageJ with plugin for stacks manipulation.

6.1 Sample quantification

The analysis of the parameters of the actual sample prepared was necessary in order to adjust the simulation. Thus, to maintain the logical structure of this text it is described in Chap. 5.3. The hydrogel sample was measured while placed in a chamber in between two cover slips immersed in PBS, similarly to the way it was during the preparation. The chamber thickness coincided with the thickness of the hydrogel strip, i. e. $800 \mu\text{m}$.



Figure 14: Hydrogel sample prepared for imaging.

From the first observation of the z-stacks captured, it was obvious that each structure needs to be cropped out and analysed separately. As listed in tab. 1, the structures were in different depth under the hydrogel surface, see fig. 15. They also were not perfectly in one line. Therefore, if we take the xz cross section of the whole z-stack, some of the structures are perfectly resolvable while others are not even visible.

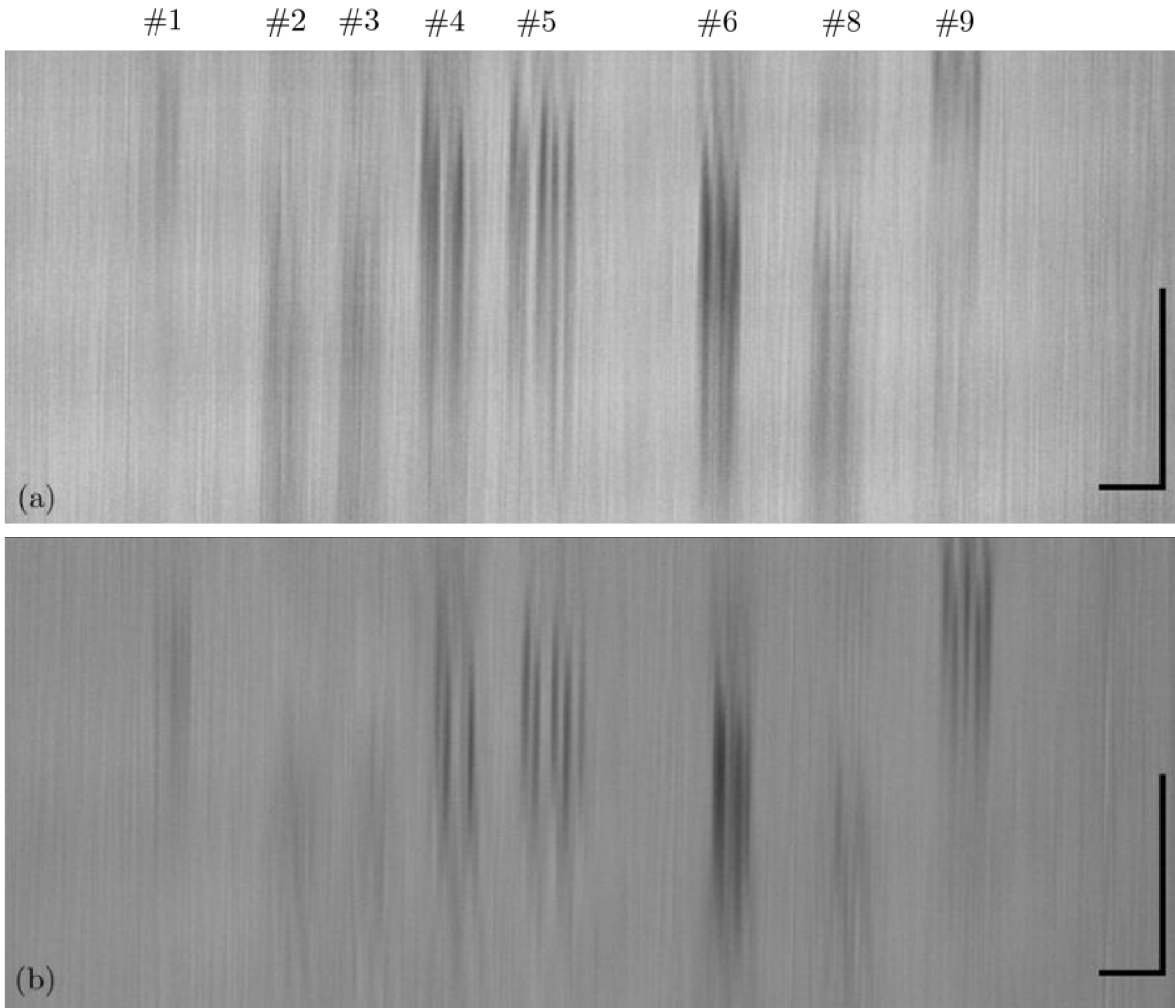


Figure 15: xz cross section of the whole hydrogel z -stack, (a) $NA_S = 0.3$, (b) $NA_S = 0.5$; scale bars $10 \mu\text{m}$; numbers of the structures shown above.

6.2 Axial localization with original condenser optics

In the beginning, the existence of the trend in axial localization improvement had to be verified and compared to the simulation and to the expectations based on the theory. The images were acquired for various numerical apertures of the illumination. The results are shown in fig. 16. In the images (a), (b) and (c) we can clearly see the trend, predicted by the simulation. While the degree of coherence decreases, the axial localization and lateral resolution improves. In fig. 16 (a), the “ghost” shadow is present, due to the high degree of coherence.

As was mentioned already in Chap. 2, for NA_S higher than approximately 0.3, the resolution no longer improves, due to the aberrations of the condensers. The difference between images (d) and (e) is caused only by movement of the hydrogel strip itself. Since it is immersed in PBS and not fixed, it floats in the chamber and does not stay in the precisely same position. Even though we can consider the lateral resolution of images (c)-(e)

the same, the axial localization seems slightly different in (e). This is most likely result of the change in the tilt of the hydrogel.

This was the starting point. Since the trend in axial localization improvement was experimentally proved, even for the low quality condenser optics, it is therefore highly expectable to achieve better results using low aberration lenses.

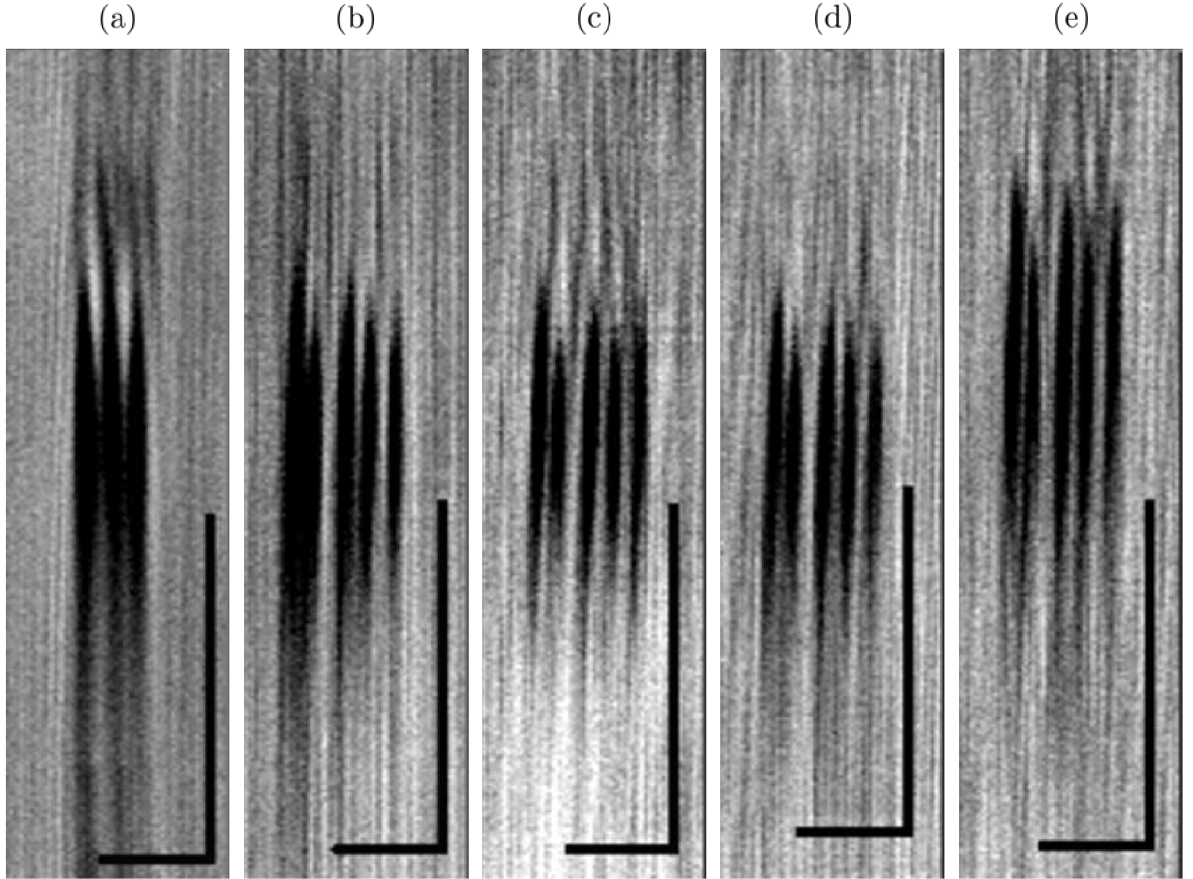


Figure 16: Structure #5, xz cross section of a z -stack, $NA = 0.5$; (a) $NA_S = 0.1$, (b) $NA_S = 0.2$, (c) $NA_S = 0.3$, (d) $NA_S = 0.4$, (e) $NA_S = 0.5$; scale bars $10 \mu\text{m}$.

6.3 Microscope adaptation for the use of condenser optics with high numerical aperture

The condensers that illuminate the specimen and reference plane in both arms have quite high aberrations, especially in the periphery of their aperture. So the effective numerical aperture of the condensers is in fact lower than nominal. The aberrations cause different phase shift of light from corresponding points of the source in the object plane in the two arms of the microscope. The light from different points within the source then causes laterally shifted interference structures in the output plane. To get rid of these, classical microscope objectives were selected as a substitution, because they are very well corrected. This makes the newly proposed design similar to the first generation of CCHM [12]

but with the difference that the same two objectives with NA high enough are used for all the possible magnifications.

According to the simulation, the increase of the NA_S of the condensers should not only improve the axial localization but it is expected to bring other positive effects as well. The holographic signal of CCHM should also increase, because the hologram will be created by the interference of light from more points of the extended source. With the original condensers, the light coming from these points negatively affected the image quality by increasing the background of the hologram. Another important effect should be the improvement of lateral resolution. All of the parameters mentioned were used to evaluate the results.

The demands on the design and technical construction and all the options considered are described here, though some of them showed out as unsuccessful. Rotation of the condensers was considered as a possible improvement method and new holders were designed that allowed for the rotation and shift of the condensers and also for exchanging the condensers for high NA microscope objectives.

6.3.1 Positioning of the condensers

Our first approach was to try to eliminate the aberrations by better mutual positioning of the condenser in the object arm and that in the reference one. The condensers, although they are supposed to be identical, may have similar aberrations but they may add up in the current mutual position. Probably a better match could be found by rotating the condensers and the aberration could even mutually correct themselves. This is mainly the purpose of the adaptation design described further. In order to have a rough idea how this will work we first tried to rotate the condensers just by unscrewing them from the current holders.

Firstly, the condenser in the reference arm was released and rotated with the object arm condenser left tightened. Unfortunately, as the condenser was moved even slightly

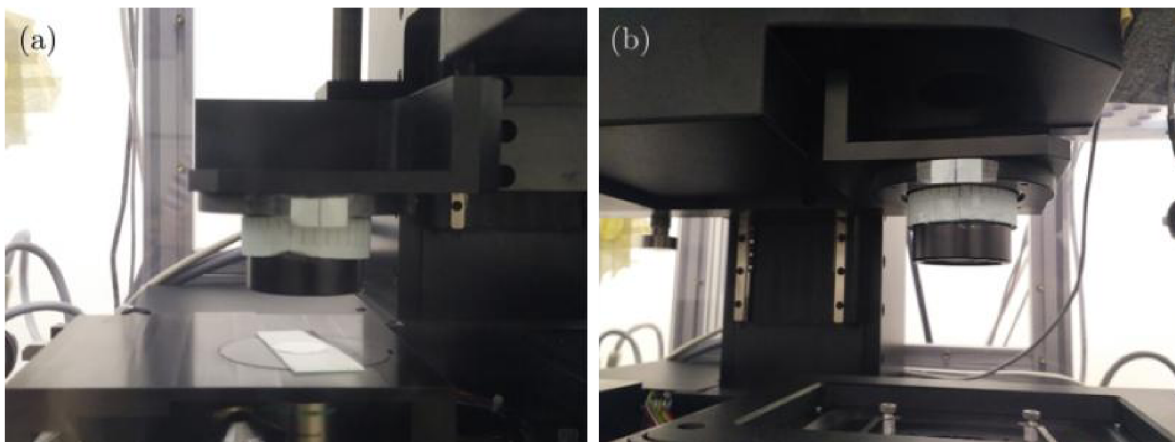


Figure 17: The scale for condenser rotation; (a) in reference arm, (b) in object arm.

from the original position, a serious obstacle for this approach appeared. Turned out, the optical setup was highly decentered and it was carefully aligned specially in the position in which it was built. Therefore, by condenser rotation the illuminated area was moving out of the field of view of the objectives.

To measure the angle of rotation, we placed a paper ring on both condensers with marks denoting 10° step, as shown in fig. 17.

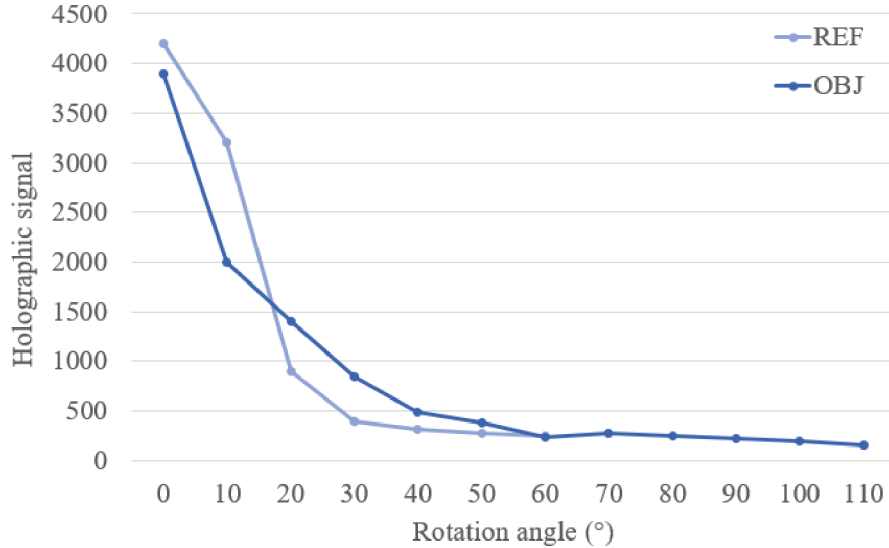


Figure 18: The decrease of holographic signal depending on the rotation angle of the condenser, REF is rotation of the condenser in the reference arm, OBJ is rotation of the condenser in the object arm.

Anyway, both the rotation of reference arm condenser and object arm condenser was tested. The procedure consisted of adjustment of the microscope for maximum holographic signal and $NA_S = 0.52$ when imaging phase USAF test chart, then rotating the condenser by 10° and adjusting the maximum signal again. It was necessary to slightly move the condenser in the loose threading to keep the light in the field of view. This positioning of the condenser, done by gentle tapping on the condenser side, is unreproducible and the position is highly unstable.

In fig. 18 the decrease of the holographic signal is plotted, showing its dependence on the rotation of both condensers. The values of holographic signal are shown in the operating software and inform about the amount of grey levels between dark and bright fringe in the 14bit digital hologram. Although it is possible to adjust the microscope for the angles up to 110° , the signal is getting very low even for a slight rotation. We found out that the system is much more sensitive to the movement of reference arm condenser, than to the object arm one. When the reference arm condenser was rotated from its original position, the signal was lost at 60° , since it was no longer possible to fit the area illuminated by the condenser to the field of view of the objective. The adjustment with the rotation of the object arm condenser was sustainable up to the angle of 110° .

As the results for condenser rotation were rather disappointing, we focused mostly on the use of microscope objectives instead of the condensers. The adapters that were designed should make the rotation and positioning of the condensers easier and this will be a task for future research.

6.3.2 The mechanical design and adaptation for objectives

The original condensers and the objectives are shown in fig. 19. In (b) the objective Nikon CFI Plan Fluor 20 × /0.5 is depicted, but of course all the Nikon objectives have the same diameter and threading and can be arbitrarily exchanged as required. Their mechanical differences were rather easy to overcome by designing a simple size adapter. The difference in their optical performance had to be studied experimentally since it was not easily predictable how the infinity-corrected objectives will serve at the position of the condensers in a system that is not optically adjusted for them. Plus, the manufacturer does not share many parameters besides the standard catalogue ones, therefore the experimental study was the only possible way of examination of their performance.

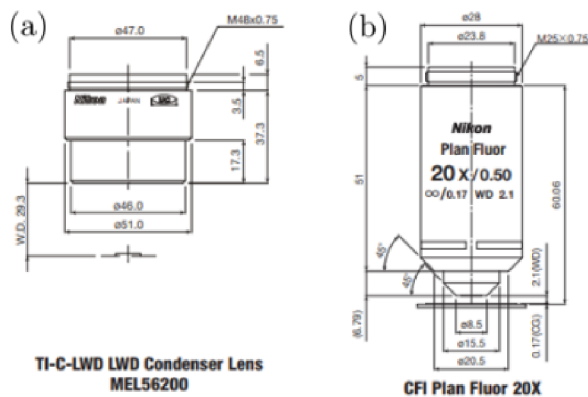


Figure 19: Comparison of mechanical parameters (a) the original condensers and (b) the objectives used as condensers after the design change [37].

Completely new holders were designed for the adjustment of the condensers but since time was limited and the first experiments with the rotation of the condensers was unsuccessful, we rather focused on other options. The mechanical designs were done in cooperation with Ing. Zbyněk Dostál, Ph.D.

The schema of the new holder with the original condenser and adapted for objective is in fig. 20 and fig. 21 respectively. The parts noted (H) are the original holders, where the condensers were fixed. In the new design, an insert is placed between the frame and the condenser that allows for free rotation and also xy shift. The ring (A) in fig. 21 is the size adapter for the use of objectives. It can also be used for the exchange of the condensers in the original holders.

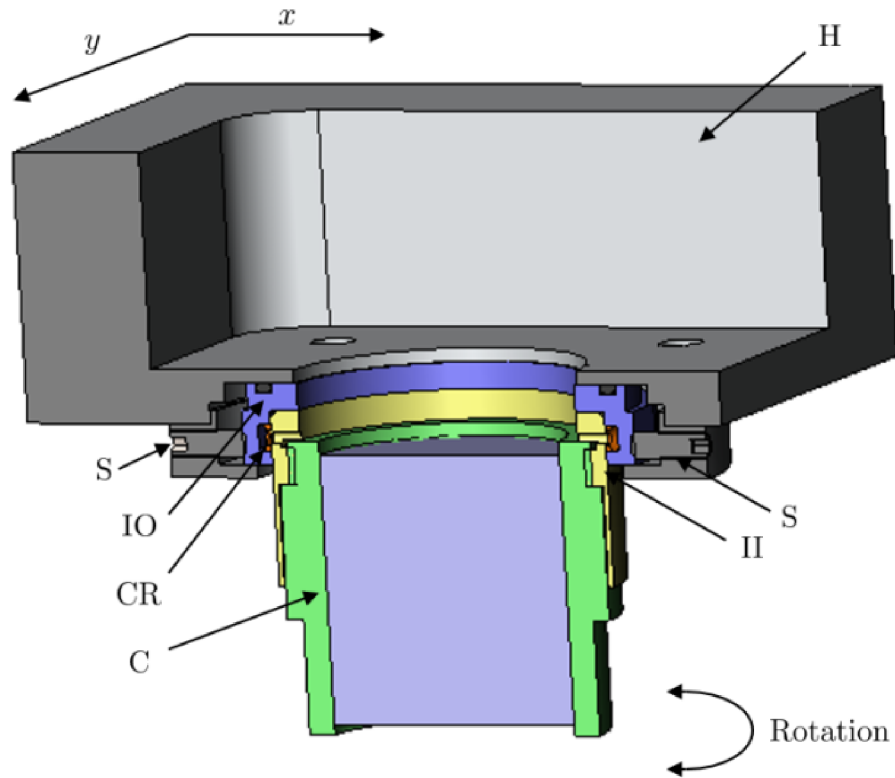


Figure 20: The novel design of the condenser holder: (H) original holder, (IO) Insert, outer part, (II) Insert, inner part, (CR) C ring, (S) screws, (C) condenser.

The insert is composed of two parts with a groove in between, where two C-rings, (CR) in the figures, are placed. Those C-rings are fixed by two screws to the inner part of the insert (II). Such arrangement allows for the inner part to be rotated freely by 360° . The lateral shift of the condenser is done by four screws (S), holding the outer part of the insert (IO) in the original holder. The insert is not fixed in the frame and by screwing or unscrewing the two opposite screws, it can be shifted either in x, y or both directions simultaneously. By this shift, it should be possible to find the right position of the condenser easily and also it would stabilize the position and enable reproducibility.

These inserts for the condenser positioning will be used in larger setup reconstruction, which is not part of this thesis. The drawings are attached to the thesis.

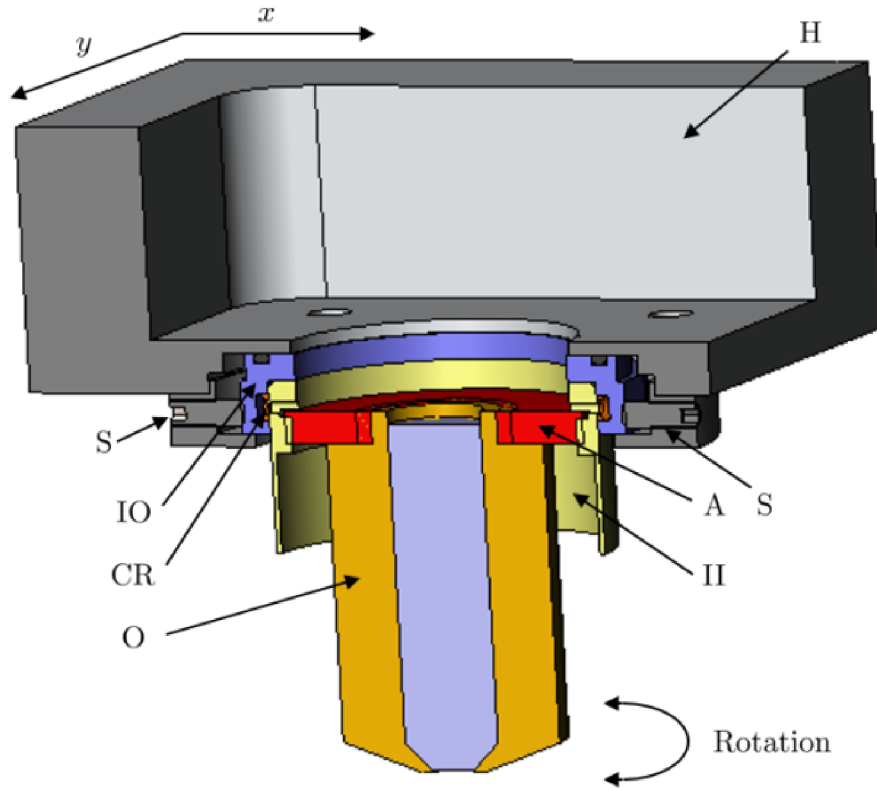


Figure 21: The novel design of the condenser holder, adapted for the microscope objective: (H) original holder, (IO) Insert, outer part, (II) Insert, inner part, (CR) C ring, (A) size adapter, (S) screws, (O) objective.

6.3.3 The 40× objectives in the condenser position

Based on the theory, it might seem that it would be best to use objectives with the highest NA possible. Therefore the first idea was to use objectives Nikon CFI Plan Fluor 40×/0.75. The imaging objectives have $NA = 0.5$, so the condenser objective with maximum aperture allows for the minimum degree of coherence.

As mentioned in Chap. 2, the original condensers have the diameter of the aperture in back focal plane around 28 mm. Obviously, see fig. 19, the objectives are much smaller in diameter and their back aperture is approximately $\varnothing 8$ mm. The image of the extended light source filled the aperture of the condensers fully. We tried to change the focus of the illumination system in order to reduce the size of the extended source image, fig. 3 in Chap. 2, but there was no simple solution such as placing a simple optical system consisting of one or two lenses between the relay lenses of the illumination system. Fortunately, the intensity of the light source and the sensitivity of the detector is high enough and we did not have any problems that would be caused by limiting the light in the system.

Since the objectives' prime purpose is not illumination, their optical performance as condensers was not quite predictable. Experimentally, it was found out, after placing the objectives in the condenser position of CCHM, that they behave in such a way that they focus the light incoming to their back aperture in a plane that is in their working distance in front of the frontal lens. The working distance of the $40\times$ objectives is 0.66 mm and this was a serious issue. The working space left between the condenser objectives and imaging objectives was then smaller than 3 mm and most of it was under the stage level. This allowed no three-dimensional imaging and even the observation of a 2D phase USAF test was difficult. The image quality was very unstable and it was really difficult to adjust the microscope. Even when adjusted as well as possible, no images in reasonable quality could be captured.

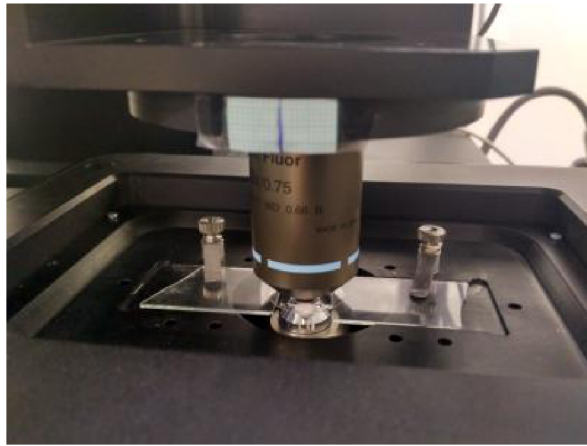


Figure 22: The $40\times/0.75$ in the position of the condensers.

The lack of working space is apparent in fig. 22. In the reference arm, the frontal lens of the condenser objective was lower than is the surface of the stage and therefore no space was left for the microscope slides, which are necessary for the height adjustment of the reference arm.

6.3.4 The final version of microscope adaptation

Two microscope objectives $20\times/0.5$ were chosen to be used instead of the original condensers after the first experiment with high NA objectives. They were identical with the objectives in the imaging part of the microscope. The illumination aperture NA_S is always limited by the smaller one of NA and numerical aperture of condensers, possibly limited also by the illumination aperture diaphragm. Therefore, in the case of same values of numerical apertures, the maximum $NA_S = NA = 0.5$. The working distance WD is 2.1 mm. This is still very little, compared to the original condensers with $WD = 29.3$ mm but it is enough for imaging samples up to approximately 1.5 mm thick.

The comparison of the two arrangements, with condensers and with objectives is in fig. 23. The reduction of the working space is obvious and is still significant. (a) and (b) compare the situation in the object arm. Although the condenser objective is very close to the sample, it does not limit the requirements for the sample thickness significantly, because samples thicker than 1.5 mm are rare anyway. The large working space we obtain by the use of the original condensers is mostly for the user's comfort with sample manipulation and has no optical advantage. This time, the microscope adjustment was successful and the imaging quality was not affected by the mechanical difficulties. In fact, it was possible to achieve even higher holographic signal with this arrangement than with the most successful adjustment with the original condensers, as it was supposed.

Therefore, the $20\times/0.5$ objectives were selected to play the role of condensers for the following experiments demonstrating the improvement in lateral resolution and axial localization.

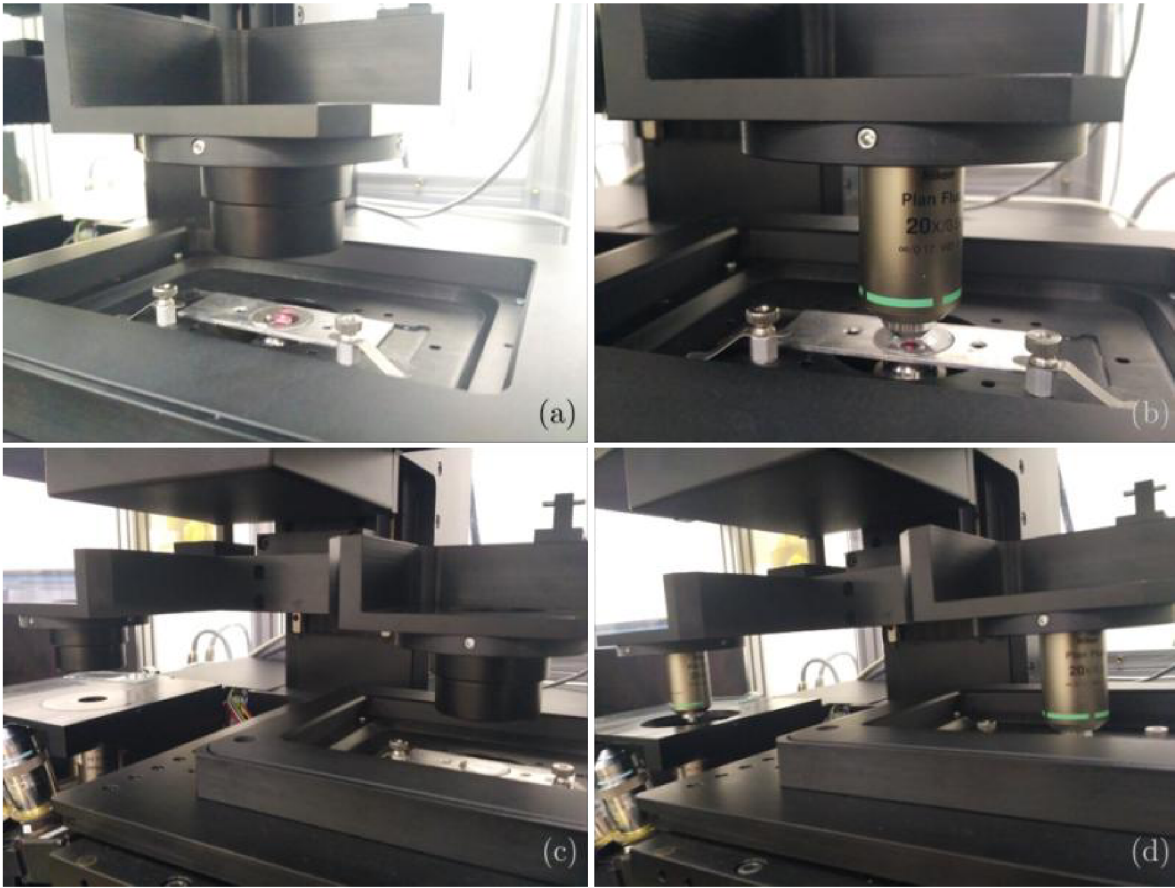


Figure 23: Condenser part of the microscope setup: (a), (c) with original condensers, (b), (d) with microscope objectives used as condensers.

6.3.5 The process of microscope adjustment

In the setup with the original condensers, the adjustment procedure is almost completely automatic, which makes it very user-friendly. When using the objectives for illumination, the whole automatic procedure could not be performed. Because the procedure is calibrated for the condensers, it might happen that the overlay in reference and object arm and subsequent interference tune would not be successful.

Luckily, the software allows to execute each step of the adjustment procedure separately. The adjustment and its adaptation for the use of condenser objectives was an important part of every experiment. By becoming familiar with the specific process, we could execute the measurements quickly, which was needed for elimination of the influence of unwanted movements of the hydrogel sample.

Each session of hydrogel measurement started by finding the structures in the strip, using the standard microscope setup. The structures were located by finding the square marks (see Chap. 5.3) and then focused with $20 \times /0.5$ imaging objectives. The system was adjusted by the usual automatic procedure. Since the imaging objectives are not influenced by the illumination system, they remained well focused on the specimen through all the next steps. The condensers could be then exchanged for the objectives without losing the focus in the specimen plane. It would be rather complicated to find and focus the hydrogel structures with the objectives, because it is impossible to adjust the microscope without focusing the specimen plane and without the adjustment, the signal was very low.

The adaptation starts with the original condensers being unscrewed from the holders. The size adapters carrying the two microscope objectives are put in their place. After that, the standard adjustment procedure is carried out, but this time step by step.

Firstly, we almost close the field diaphragm (FA) (see fig. 3) and focus its image on the specimen, with the reference arm closed, so no light from it arrives to the detector. Then the object arm is closed and microscope slides or cover slips are put in the reference arm, to balance the thickness of the object. The precise focus in the reference is achieved by changing the relative focus via a software setting. After focusing both arms, the field aperture is opened.

The following steps belong to the automatic adjustment procedure, but they were used separately while constantly checking if the imaging quality is still increasing. The order is:

1. Image overlay - may be fine-tuned manually, but usually performs well. It uses a pinhole to precisely overlay the image from object and reference arm.
2. Interference tune - extra fine tune is the most precise, but while using the objectives instead of the condensers, it tends to fall into some local maximum and the tune is then unsuccessful. This may be solved by using the coarse tune. This step is finding the right length of the reference beam path in order to achieve the highest contrast of the interference fringes.

3. Smart scan - for better reference arm alignment. It is an algorithm searching for the maximum of holographic signal.
4. Auto-signal - helps to maintain the best adjustment, may be used also in between the measurements.

Last step of the automatic adjustment procedure is Z-scan. This function searches for the best focus but in our case it causes the loss of the focus in the plane with the hydrogel structures. Thus it is necessary to execute each automatic step manually and avoid the change of Z-position.

6.4 Improvement in lateral resolution

After the mechanical adaptation of the microscope setup, the first task was to check, whether the condenser objectives work as the theory suggest. Since the maximum illumination numerical aperture increased from 0.3 to 0.5, we expected to see improvement in lateral resolution.

The theoretical cut-off frequency is given by $f_{\text{MAX}} = (\text{NA} + \text{NA}_{\text{S}})/\lambda$ [3]. For $\text{NA}_{\text{S}} = 0.3$, i. e. the original condensers, the frequency $f_{\text{C}} = 1.230 \cdot 10^3 \text{ mm}^{-1}$ and for the condenser objectives with $\text{NA}_{\text{S}} = 0.5$ enhances to $f_{\text{O}} = 1.538 \cdot 10^3 \text{ mm}^{-1}$. We expected to almost reach the technical limit of resolution of the microscope.

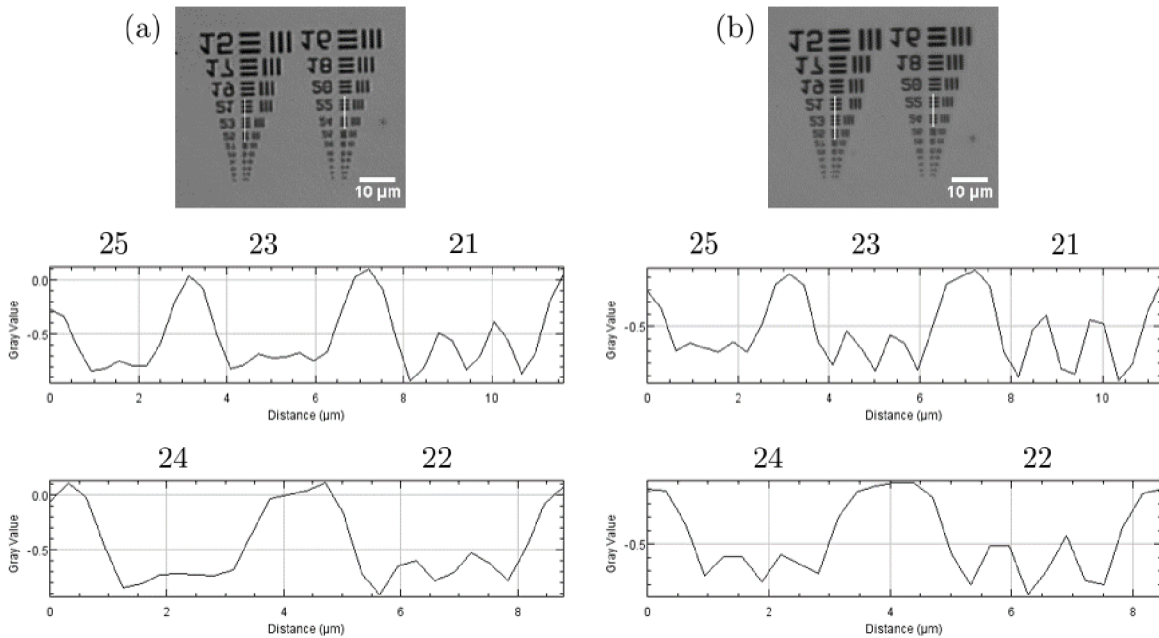


Figure 24: Comparison of lateral resolution measured on phase USAF test, $\text{NA} = 0.5$: left (a) original condensers, $\text{NA}_{\text{S}} = 0.3$, last resolvable structure is pattern #22; right (b) objectives used as condensers, $\text{NA}_{\text{S}} = 0.5$, last resolvable structure is pattern #24.

We observed the part of the phase USAF-like test with the smallest spatial frequencies, fringe pattern noted #15 to #37. In fig. 24 is the comparison of patterns number #21 - #25. Left, (a) is an image captured with $\text{NA}_S = 0.3$ and image for $\text{NA}_S = 0.5$ is on the right side (b). Under the images the intensity along the white lines (across the fringe patterns) is plotted. The frequencies of the fringes are in tab. 2.

As we see in fig. 24, the last resolvable structure in (a) is #22 with frequency $f_{22} = 0.942 \cdot 10^3 \text{ mm}^{-1}$. With lower spatial coherence of illumination, (b), we resolve pattern #24 with $f_{24} = 1.160 \cdot 10^3 \text{ mm}^{-1}$ and with better contrast we might resolve #25 with $f_{25} = 1.287 \cdot 10^3 \text{ mm}^{-1}$. The low contrast of the images is most likely the reason why the resolution does not reach its theoretical limit. When the series of three fringes is imaged to less than seven pixels of the detector, the contrast is too low and they disappear in similar shades of grey. The same happens to pattern #23 in (a), where it theoretically should be resolved but it again fades in the low contrast.

Pattern	#21	#22	#23	#24	#25	#26	#27
Frequency ($10^3 \cdot \text{mm}^{-1}$)	0.848	0.942	1.045	1.160	1.287	1.429	1.585

Table 2: Frequency of the selected USAF test patterns.

The frequency of pattern #25 is close to the Nyquist frequency, i. e. the resolution limit. We successfully confirmed that the lateral resolution increased with higher numerical aperture NA_S . It is not the aim of this thesis to study the lateral resolution conditions in detail.

6.5 Improvement in axial localization

Similar measurement as in Chap. 6.2 was performed with the objectives in the condenser position. Since the software is designed for the use of condensers with back aperture $\varnothing 28 \text{ mm}$, the slider that controls the NA_S was no longer showing the true aperture. We estimated that the back aperture of the objectives, $\varnothing 8 \text{ mm}$, is filled for the slider set to 0.16. Hence, a shift of the slider by 0.03 equals to the change of NA_S by 0.1.

The results are displayed in fig. 25 for the full range of NA_S plus the situation with the aperture opened to its maximum (g). We can clearly see that the trend of axial localization improvement for decreasing degree of coherence, predicted by the simulations (Chap. 5) and verified by the experiment with the condensers, is again present here. Both the lateral resolution and axial localization is improved. In (f) and (g) we can distinguish the elements of the structure in x direction. We also see their mutual shift in z direction - two of them are lower than the other three. It is possible to estimate their mutual shift, which is about $5 \mu\text{m}$ as it should be. Due to considerably low NA and NA_S , even though it improved a lot, the elements are still axially prolonged and appear longer than they are in reality. It appears that for the maximum aperture (fig. 25 (g)), the resolution improves even a bit more, which probably means that the full back aperture of the condenser objectives was not estimated completely right.

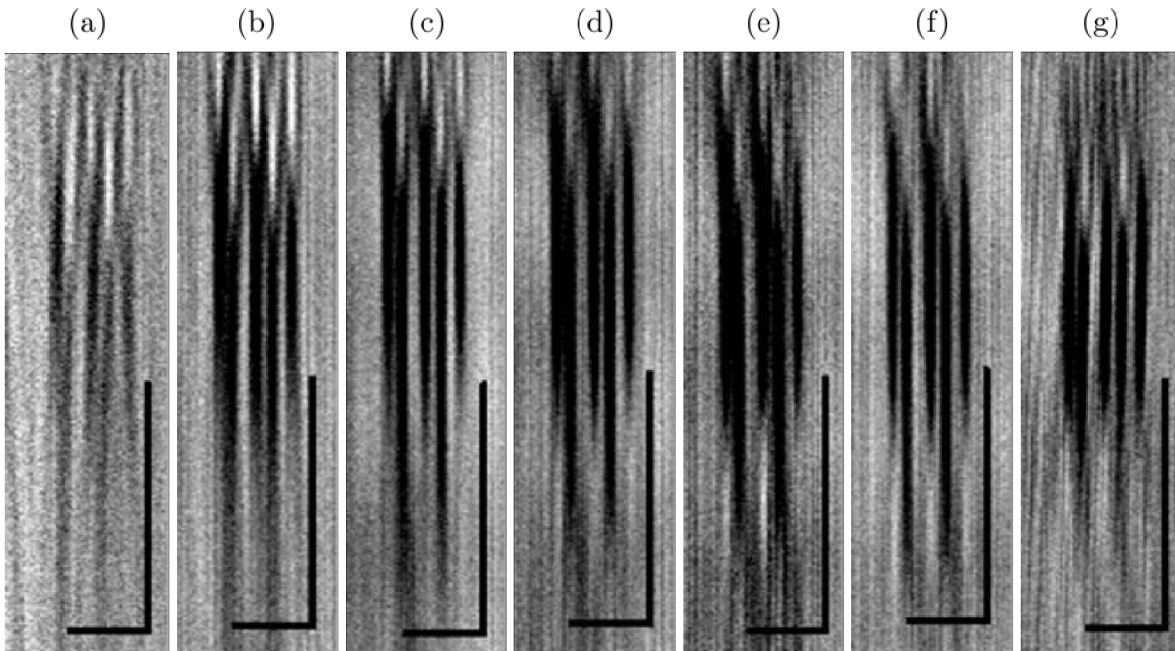


Figure 25: Structure #5, xz cross section of a z-stack, $NA = 0.5$, objectives used as condensers, NA_S stands for the estimated real value, the number in brackets is the software setting; (a) $NA_S = 0.1$ (0.03), (b) $NA_S = 0.2$ (0.06), (c) $NA_S = 0.3$ (0.09), (d) $NA_S = 0.4$ (0.12), (e) $NA_S = 0.45$ (0.14), (f) $NA_S = 0.5$ (0.16), (g) $NA_S = \text{MAX}$ (0.52); scale bars $10 \mu\text{m}$.

The first image on the left, for very coherent illumination, is severely affected by the fact that almost no light is transmitted through the system. Even so, in (a) and (b), we again observe the “ghost” shadows that we know from the simulation. Fortunately, the hydrogel stayed in the same position through all the z-stacks captured, which allows for the comparison of the xz cross sections.

Next, fig. 26 displays the comparison of structures #5, #6, #8 and #9 from z-stacks taken for (a) the best achievable adjustment with the original condensers and (b) the best adjustment with the objectives used as condensers. Here it is apparent that the elements that are spaced $4 \mu\text{m}$ from each other and closer are not resolved by the microscope, but the trend of improvement is seen in them as well. See Chap. 5 for the details about the structure parameters.

Another issue with the hydrogel strip, besides moving during the experiment, was its tilt. The strip was very narrow and the cut edges were very rough, therefore it did not lay flat on the bottom cover slip but it was slightly tilted. Although this tilt is not that apparent in zy cross section, fig. 28 - 29, of any of the z-stacks, it causes trouble when comparing the xz cross sections. This problem is illustrated in fig.27. For the same cases as in fig.26, (a) for $NA_S = 0.3$ and (b) for $NA_S = 0.5$, seven following xz cross sections are shown. Each is one pixel shifted in y position from the previous one. Apparently, the tilt is mostly in the y direction and it seems to be the same in both (a) and (b). In fact, in the image analysis it appeared that the tilt is very similar for all the z-stacks and so

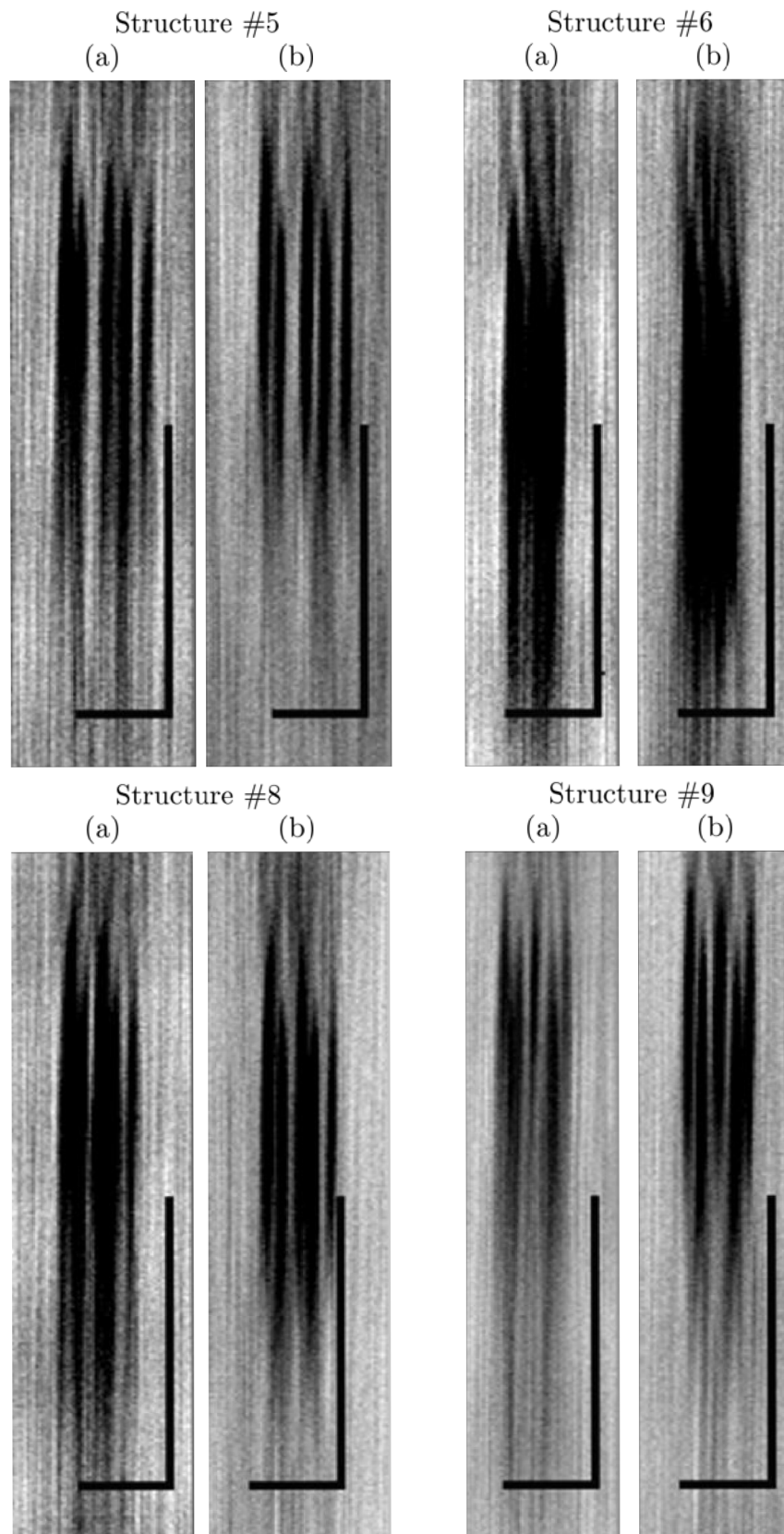


Figure 26: Comparison of selected structures of the sample, (a) $NA_S = 0.3$, (b) $NA_S = 0.5$; scale bars $10 \mu\text{m}$.

we may assume that this is the most stable position of the hydrogel strip. Thanks to that we may compare the images although the sample might have slightly moved between the z-stack acquisitions.

Let's take a closer look at fig. 28 and 29. Images (a) - (e) depict the zy cross sections through each element of structure #5, for $\text{NA}_S = 0.5$ and $\text{NA}_S = 0.3$, respectively. In fig. 28, we can clearly distinguish between the upper (fig. 28 (b), (d)) and the bottom (fig. 28 (a), (c), (e)) row of the structure elements. We can estimate that the centres of the elements in both rows are shifted by $5 \mu\text{m}$, which corresponds with the real values (see Chap. 5.3, tab. 1). When measuring the length of the elements in the z direction, we get the average value of approximately $10 \mu\text{m}$ for imaging with $\text{NA}_S = 0.5$. Given that the real length of the element is around $7 \mu\text{m}$ and the axial length predicted by the simulation is $10 - 14 \mu\text{m}$, it seems that the imaging performs quite well. For $\text{NA}_S = 0.3$ (fig. 29), the length is roughly $13 - 14 \mu\text{m}$, so the difference between the real and image values is bigger and the elements are prolonged in the axial direction, which makes the axial localization less accurate. Also, the overall image quality is lower, so there is in fact real improvement when we increase NA_S from 0.3 to 0.5. The zy cross sections are the most convincing and the measurements in them allow us to acquire more accurate results, because unlike the xz cross sections, they show the real length of the phase images of the elements. However, the xz cross sections display the improvement in lateral resolution and axial localization simultaneously.

It may seem, especially when comparing the xz images in fig. 27, that the localization improvement is not that significant and it is rather the improvement in lateral resolution that helps us to resolve the structure. This is probably highly affected by the instability of the hydrogel strip and though many series of z-stack image acquisition were carried out, for various NA_S , it was impossible to decide what exactly causes the image quality improvement. Most likely, both effects play their role and, for sure, the impact of low coherence needs to be further studied using more stable specimen.

Finally, let's summarize and discuss the results. Even though the structures in hydrogel are tilted, their parameters were measured in the zy cross sections (fig. 28) and therefore these sections carry the true information about the size of the structures despite of their tilt. The axial length and mutual position of the elements is clearly visible in the zy views. The xz cross sections (fig. 15) are affected by the tilt and in fact never show the elements in full length and so they cannot be reliably used for measurement. They are useful for visual display and are more practical for comparison of images taken with different NA_S .

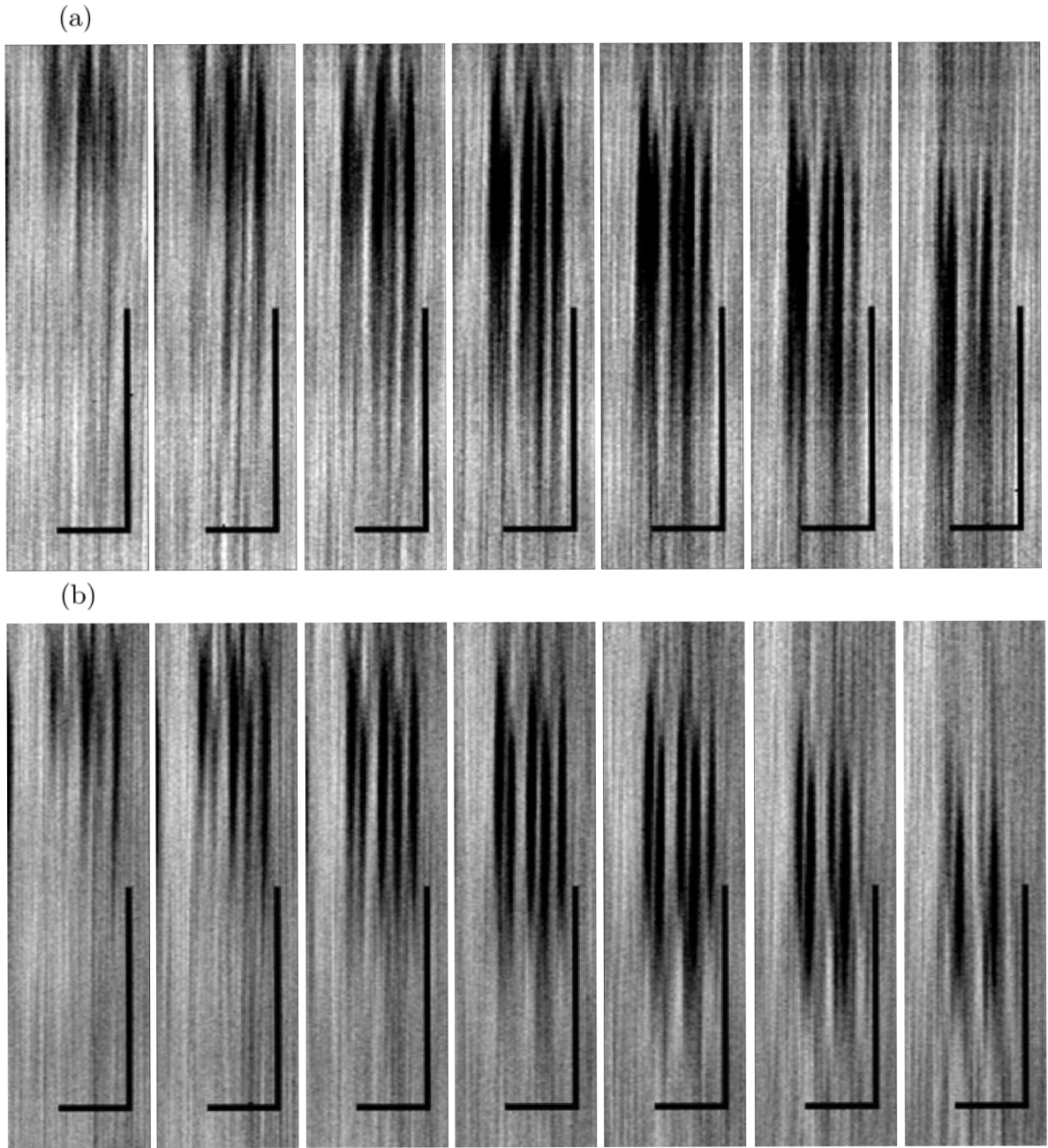


Figure 27: Series of seven following xz cross sections of the z -stacks, structure #5, (a) for $NA_S = 0.3$, (b) for $NA_S = 0.5$; scale bars $10 \mu\text{m}$.

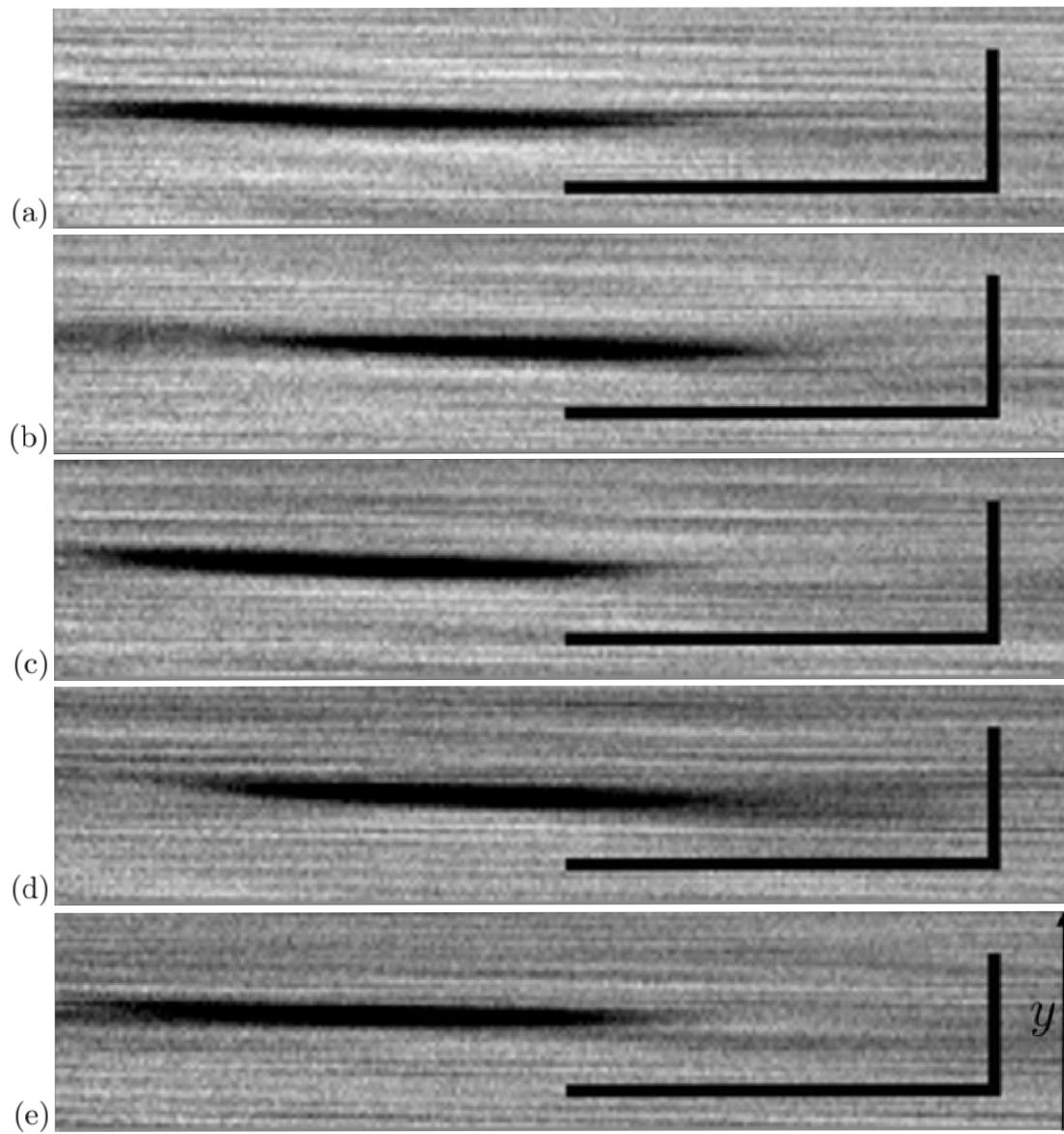


Figure 28: Series of zy cross section of a z -stack, each through one structure element, $NA_S = 0.5$: (b) and (d) the two elements in the upper row, (a), (c), (e) the three in the bottom one; scale bars $10 \mu\text{m}$.

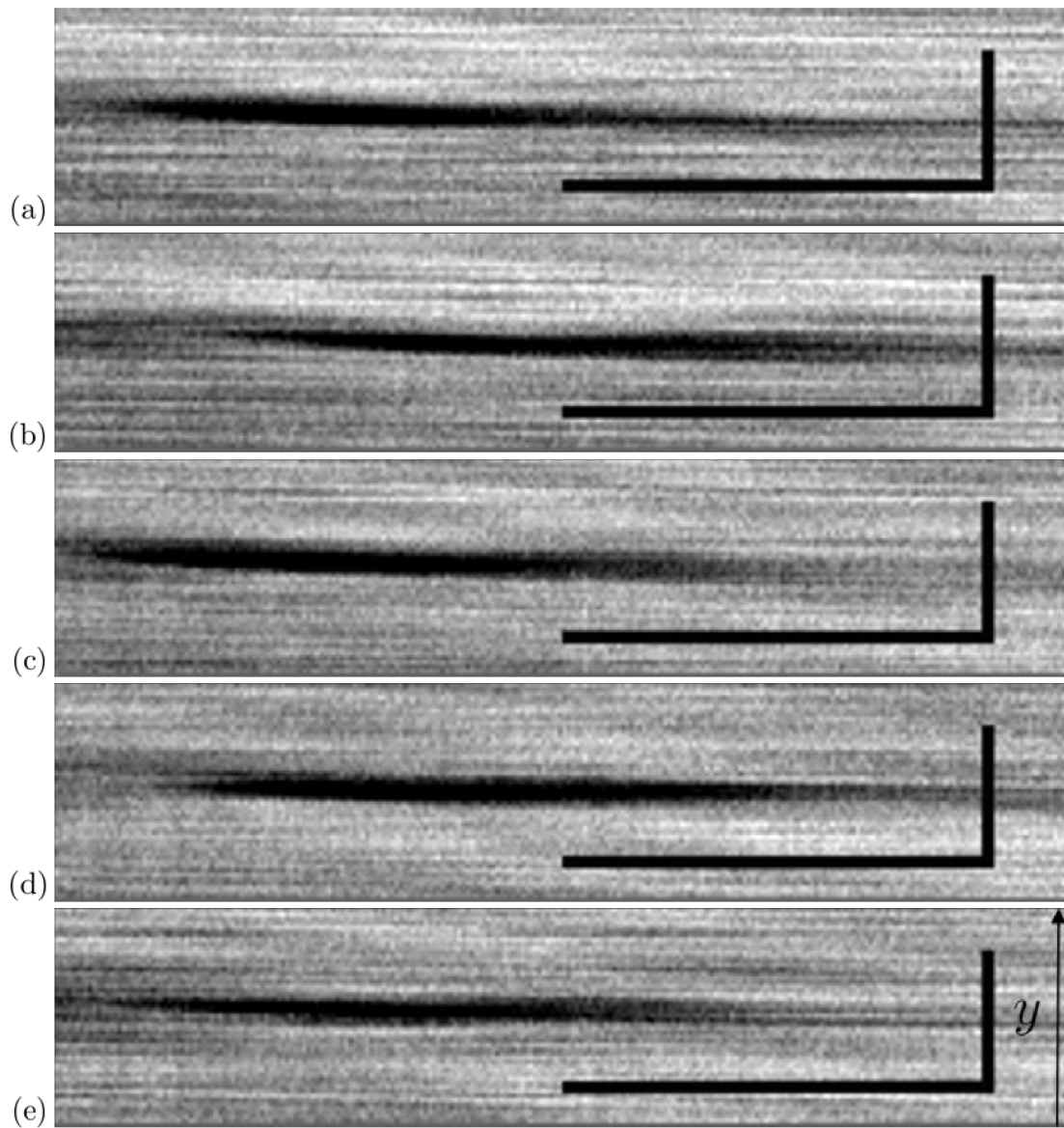


Figure 29: Series of zy cross section of a z -stack, each through one structure element, $NA_S = 0.3$: (b) and (d) the two elements in the upper row, (a), (c), (e) the three in the bottom one; scale bars $10\ \mu\text{m}$.

Conclusion

The aim of this master thesis was mainly to demonstrate the relationship between the spatial coherence of illumination numerical aperture and the imaging qualities of coherence-controlled holographic microscope, namely the lateral resolution and the capability of axial localization.

In Chapters 1 - 4, the theoretical background as well as the motivation for this study are discussed. Chap. 5 demonstrates the simulation results and the expectation that are based on the theory from Chap. 4. The last part (Chap. 6) brings the description of all the approaches that lead to the final results.

The goals of the thesis were met, although some issues of the planned approach appeared during the work. The simulations were calculated for both the theoretical model and the specific case of our sample and the trend of axial localization improvement was demonstrated on them.

Specialized mechanical holders for the microscope's condensers were designed that allow the rotation around the z axis and the x, y shift and the use of high NA optics. However, the positioning of the condensers was more difficult than expected due to the optical decentration of the whole microscope setup. A series of experiments was performed to verify the theoretical and simulated results. For this purpose, a reference hydrogel sample has been prepared, with properties resembling the simulation.

The condenser optics with high numerical aperture and low aberration was successfully tested. This approach is based on the second generation CCHM setup but it used microscope objectives as condensers, similarly to the first generation. This brings back the main disadvantage of the previous generation of CCHM, which is the limited working space between the illumination objectives and the imaging objectives. We propose that this problem could be solved by designing some sort of specialized condenser optics for the particular holographic microscope. The microscope adaptation was designed and will be useful in further research. The new condenser holders allow for the use of either the original condensers or the microscope objectives as condensers. Since it also enables the rotation of the condensers and precise xy shift, we were able to establish a reliable and reproducible procedure for the microscope adjustment.

The theoretical results of the simulation were mostly verified in the last Chap. 6. The trend of improvement in axial localization, which results from the decrease of spatial coherence of illumination, was proven successfully. Unfortunately, the microscope images (xz cross sections) are not well-comparable to the simulation images. But the values from the zy cross sections correspond to those of the simulations. The improvement of lateral resolution was confirmed and now it almost reaches the technical and theoretical limit. The axial localization improved as well and the parameters of the images of the structures were comparable to the real values. The holographic signal quality of the hologram in general also improved. The theoretical expectations were therefore successfully verified.

Some issues arose from the unexpected instability of the reference sample used. For the future research on this topic, we suggest to use chalcogenide glass or similar material for the sample preparation. It is solid and therefore more stable. It also does not need to be immersed. Yet it is still possible to modify small areas within this material, similarly to the procedure performed on the hydrogel.

To sum up, the primary research on the dependence of axial localization on spatial coherence was carried out and the important steps are described in this thesis. We hope that this will serve as a basis for further studies. One day it might contribute to the improvement of three-dimensional quantitative phase imaging in general.

References

- [1] JANEČKOVÁ, H., VESELÝ, P. CHMELÍK, R.: Proving tumour cells by acute nutritional/energy deprivation as a survival threat: a task for microscopy. *ANTICANCER RESEARCH*, vol. 29, no. 6, 2009: pp. 2339–2346, ISSN 0250-7005, Available from: doi:10.1.1.846.9506.
- [2] JANEČKOVÁ, H. et al.: Digital holographic microscope with low spatial and temporal coherence of illumination. In *Photonics Europe*, vol. 7000, International Society for Optics and Photonics, 2008, pp. 70002E–70002E., Available from: doi:10.1117/12.800392.
- [3] CHMELÍK, R. et al.: Holographic microscopy in low coherence. In *QUANTITATIVE PHASE IMAGING II*, SPIE, 2016, ISBN 978-1-62841-952-8, pp. 971806–7, Available from: doi:10.1117/12.2209465.
- [4] ABBE, E.: Beitrage zur Theorie des Mikroskops und der mikroskopischen Wahrnehmung. *Archiv fur mikroskopische Anatomie*, vol. 9, no. 1, 1873: pp. 413–418, ISSN 0176-7364, Available from: doi:10.1007/BF02956173.
- [5] POPESCU, G.: *Quantitative phase imaging of cells and tissues*. McGraw-Hill, 2011, ISBN 978-0-07-166343-4.
- [6] ZERNIKE, F.: Phase contrast, a new method for the microscopic observation of transparent objects. *Physica*, vol. 9, no. 7, 1942: pp. 686–698, ISSN 00318914, Available from: doi:10.1016/S0031-8914(42)80035-X.
- [7] NOMARSKI, G.: Differential micointerferometer with polarised waves. *J. Phys. Radium, Paris*, vol. 16, no. 9, 1955: pp. 9S–13S.
- [8] GABOR, D.: A New Microscopic Principle. *Nature*, vol. 161, 5 1948: pp. 777–778, Available from: doi:10.1038/161777a0.
- [9] GABOR, D.: Holography, 1948 - 1971. *Nobel Lectures, Physics 1971 - 1980*, .Singapore: World Scientific Publishing, 1992.
- [10] LEITH, E. N. UPATNIKES, J.: Reconstructed Wavefronts and Communication Theory. *J. Opt. Soc. Am.*, vol. 52, no. 10, 10 1962: pp. 1123–1130., Available from: doi:10.1364/JOSA.52.001123.
- [11] SLABÝ, T. et al.: Coherence-controlled holographic microscopy for live-cell quantitative phase imaging. In *Quantitative Phase Imaging*, ed. by G. Popescu; Y. Park, SPIE, 3 2015, ISBN 978-1-62841-426-4, pp. 93360K–4, Available from: doi:10.1117/12.2080128.

- [12] KOLMAN, P. CHMELÍK, R.: Coherence-controlled holographic microscope. *Opt. Express*, vol. 18, no. 21, 10 2010: pp. 21990–22003, ISSN 1094-4087, Available from: doi:10.1364/OE.18.021990.
- [13] SLABÝ, T. et al.: Off-axis setup taking full advantage of incoherent illumination in coherence-controlled holographic microscope. *Opt. Express*, vol. 21, no. 12, 6 2013: pp. 14747–14762, ISSN 1094-4087, Available from: doi:10.1364/OE.21.014747.
- [14] CHMELÍK, R.: Three-dimensional scalar imaging in high-aperture low-coherence interference and holographic microscopes. *JOURNAL OF MODERN OPTICS*, vol. 53, no. 18, 12 2006: pp. 2673–2689, Available from: doi:10.1080/09500340600828541.
- [15] CHMELÍK, R. et al.: The Role of coherence in Image Formation in Holographic Microscopy. *PROGRESS IN OPTICS*, vol. 59, no. 1, 2014: pp. 267–336, ISSN 0079-6638, Available from: doi:10.1016/B978-0-444-63379-8.00005-2.
- [16] DUBOIS, F. YOURASSOWSKY, C.: Full off-axis red-green-blue digital holographic and microscope with LED and illumination. *OPTICS LETTERS*, vol. 37, no. 12, 2012: pp. 2190–2192, Available from: doi:10.1364/OL.37.002190.
- [17] KÖHLER, A.: Ein neues Beleuchtungsverfahren für mikrophotographische Zwecke. *Zeitschrift für wissenschaftliche Mikroskopie und mikroskopische Technik*, vol. 10, 1893: pp. 433–440.
- [18] DOSTÁL, Z. et al.: Automated alignment method for coherence-controlled holographic microscope. *JOURNAL OF BIOMEDICAL OPTICS*, vol. 20, no. 11, 2015: pp. 111215–8., ISSN 1083-3668, Available from: doi:10.1117/1.JBO.20.11.111215.
- [19] LEITH, E. N. UPATNIKES, J.: Holography with Achromatic-Fringe Systems. *J. Opt. Soc. Am.*, vol. 57, no. 8, 8 1967: pp. 975–980., Available from: doi:10.1364/JOSA.57.000975.
- [20] SLABÝ, T. et al.: Coherence-controlled holographic microscope. In *Proc. SPIE*, vol. 22, 2 2010, ISBN 9780819482365, pp. 4180–4195, Available from: doi:10.1364/OE.22.004180.
- [21] CHMELÍK, R. HARNA, Z.: Parallel-mode confocal microscope. *OPTICAL ENGINEERING*, vol. 38, no. 10, 1999: pp. 1635–1639, Available from: doi:10.1117/1.602217.
- [22] KREIS, T.: Digital holographic interference-phase measurement using and the Fourier-transform and method. *J. Opt. Soc. Am.*, vol. 3, 1986: pp. 847–855, Available from: doi:10.1364/JOSAA.3.000847.

- [23] INDEBETOUW, G. KLYSUBUN, P.: Space-time digital holography: A three-dimensional microscopic imaging scheme with an arbitrary degree of spatial coherence. *Applied Physics Letters*, vol. 75, no. 14, 10 1999: pp. 2017–2019, Available from: doi:10.1063/1.124901.
- [24] LEITH, E. N. et al.: Optical sectioning by holographic coherence imaging: a generalized analysis. *J. Opt. Soc. Am.*, vol. 20, no. 2, 2 2003: pp. 380–387, Available from: doi:10.1364/JOSAA.20.000380.
- [25] LOŠŤÁK, M. et al.: Diffuse light imaging with a coherence controlled holographic microscope. *Proc. SPIE*, vol. 7746, 2010: pp. 77461N–77461N–9, Available from: doi:10.1117/12.882198.
- [26] DUBOIS, F. et al.: Digital Holographic Microscopy Working with a Partially Spatial Coherent Source. *Coherent Light Microscopy*, vol. 46, 11 2011: pp. 31–59, Available from: doi:10.1007/978-3-642-15813-1_2.
- [27] LOŠŤÁK, M. et al.: Coherence-controlled holographic microscopy in diffuse media. *Opt. Express*, vol. 22, no. 4, 2 2014: pp. 4180–4195, ISSN 1094-4087, Available from: doi:10.1364/oe.22.004180.
- [28] ČOLLÁKOVÁ, J. et al.: Coherence-controlled holographic microscopy enabled recognition of necrosis as the mechanism of cancer cells death after exposure to cytopathic turbid emulsion. *JOURNAL OF BIOMEDICAL OPTICS*, vol. 11, 2015: pp. 111213–1 (111213–7 s.), ISSN 1083-3668, Available from: doi:10.1117/1.JBO.20.11.111213.
- [29] KOLLÁROVÁ, V. et al.: Quantitative phase imaging through scattering media by means of coherence-controlled holographic microscope. *JOURNAL OF BIOMEDICAL OPTICS*, vol. 20, no. 11, 2015: pp. 1112016–8, ISSN 1083-3668, Available from: doi:10.1117/1.JBO.20.11.111206.
- [30] HECHT, E.: *Optics*. Addison-Wesley, 2002, ISBN 9780805385663.
- [31] BORN, M. WOLF, E.: *Principles of Optics*. Cambridge University Press, seventh expanded edition edition, 2002, ISBN 978-0521642224, Available from: doi:10.1017/CBO9781139644181.001.
- [32] PEŘINA, J. MIŠTA, L.: Definitions of Coherence Time, Coherence Area and Coherence Volume for Superposed Coherent and Chaotic Radiation. *Optica Acta: International Journal of Optics*, vol. 21, no. 4, 1974: pp. 329–340, Available from: doi:10.1080/713818895.
- [33] DUBOIS, F., JOANNES, L. LEGROS, J.-C.: Improved three-dimensional imaging with a digital and holography microscope with a source of partial and spatial coherence. *APPLIED OPTICS*, vol. 38, 1999: pp. 7085–7094, Available from: doi:10.1364/AO.38.007085.

- [34] RYTOV, S. M.: Diffraction of light by ultrasonic waves. *Izv. Akad. Nauk. SSSR ser. fiz.2*, 223, 1937.
- [35] CHMELÍK, R. et al.: Závěrečná zpráva k objednávce č. MEDINS-2017-0054-Z-MPL. 2017.
- [36] GANDARA-MONTANO, G. A. et al.: Large optical phase shifts in hydrogels written with femtosecond laser pulses: elucidating the role of localized water concentration changes. *Opt. Mater. Express*, vol. 7, no. 9, Sep 2017: pp. 3162–3180, Available from: doi:10.1364/OME.7.003162.
- [37] Nikon Corp. [Online], 2018 [2018-04-12]. Available on: www.nikon.com.